



Stochastic porous media modeling and high-resolution schemes for numerical simulation of subsurface immiscible fluid flow transport

Eric Thompson Brantson¹ · Binshan Ju^{1,2} · Dan Wu³ · Patricia Semwaah Gyan⁴

Received: 10 July 2017 / Accepted: 24 March 2018 / Published online: 7 April 2018
© Institute of Geophysics, Polish Academy of Sciences & Polish Academy of Sciences 2018

Abstract

This paper proposes stochastic petroleum porous media modeling for immiscible fluid flow simulation using Dykstra–Parson coefficient (V_{DP}) and autocorrelation lengths to generate 2D stochastic permeability values which were also used to generate porosity fields through a linear interpolation technique based on Carman–Kozeny equation. The proposed method of permeability field generation in this study was compared to turning bands method (TBM) and uniform sampling randomization method (USRM). On the other hand, many studies have also reported that, upstream mobility weighting schemes, commonly used in conventional numerical reservoir simulators do not accurately capture immiscible displacement shocks and discontinuities through stochastically generated porous media. This can be attributed to high level of numerical smearing in first-order schemes, oftentimes misinterpreted as subsurface geological features. Therefore, this work employs high-resolution schemes of SUPERBEE flux limiter, weighted essentially non-oscillatory scheme (WENO), and monotone upstream-centered schemes for conservation laws (MUSCL) to accurately capture immiscible fluid flow transport in stochastic porous media. The high-order schemes results match well with Buckley Leverett (BL) analytical solution without any non-oscillatory solutions. The governing fluid flow equations were solved numerically using simultaneous solution (SS) technique, sequential solution (SEQ) technique and iterative implicit pressure and explicit saturation (IMPES) technique which produce acceptable numerical stability and convergence rate. A comparative and numerical examples study of flow transport through the proposed method, TBM and USRM permeability fields revealed detailed subsurface instabilities with their corresponding ultimate recovery factors. Also, the impact of autocorrelation lengths on immiscible fluid flow transport were analyzed and quantified. A finite number of lines used in the TBM resulted into visual artifact banding phenomenon unlike the proposed method and USRM. In all, the proposed permeability and porosity fields generation coupled with the numerical simulator developed will aid in developing efficient mobility control schemes to improve on poor volumetric sweep efficiency in porous media.

Keywords Permeability and porosity fields · Turning bands method · Carman–Kozeny equation · SUPERBEE flux limiter · Monotone upstream-centered schemes for conservation laws · Weighted essentially non-oscillatory schemes

✉ Eric Thompson Brantson
ericthompson785@yahoo.com

✉ Binshan Ju
jubs2936@163.com

Dan Wu
wudan52087@126.com

Patricia Semwaah Gyan
triciagyan@gmail.com

² Key Laboratory of Marine Reservoir Evolution and Hydrocarbon Accumulation Mechanism, Ministry of Education, China University of Geosciences (Beijing), Beijing, China

³ Patent Examination Cooperation Centre, SIPO, Beijing 100081, China

⁴ Faculty of Earth Resources, China University of Geosciences, Wuhan 430074, China

¹ School of Energy Resources, China University of Geosciences (Beijing), Beijing 100083, China

Introduction

In reality, it is impossible to physically sample at every infinitesimal point in space in a geological porous media for reservoir fluid flow analyses. Hence, Monte Carlo simulations in geostatistics and numerical reservoir simulation are commonly used to create numerous numbers of realizations over a grid mesh to predict future reservoir fluid flow performance and uncertainty quantification. However, Dubrule (1988) and Haldorsen and Damsleth (1990) carried out a number of stochastic modeling on discrete (Markov fields, two-point histograms, truncated random functions, and Boolean schemes), continuous (fractals, universal and indicator kriging, random Gaussian fields) and hybrid approach of both techniques. Moreover, the continuous type of stochastic models are generally suitable for modeling the spatial distribution of petrophysical properties with an assumption of more or less stationarity (Haldorsen and Damsleth 1990). But, Gaussian (Deutsch and Journel 1992) and continuous spectral methods (Shinozuka and Jan 1972) are the most widely used approximate algorithms for generating numerical geological model architectures. However, TBM (Matheron 1973) as one of the oldest methods is also used for simulating spatially correlated multidimensional random field which is still rarely used in geostatistical and numerical simulation applications (Emery and Lantuéjoul 2006). The TBM and USRM (Sabelfeld 1991) was considered in this study for immiscible fluid flow transport. Furthermore, the characterization of heterogeneous petroleum reservoirs using geostatistical tools and stochastic simulation methods are often preferred to traditional interpolation techniques in which hydrocarbon fluids are transported. With regards to this assertion, Lake and Malik (1993) compared deterministic and conditional simulation results and came to the conclusion that, conditional simulation must be tailored to specific geological environment to be in a reliable agreement with deterministic simulation. All these techniques permit accurate capture of internal heterogeneous fine-scale details and quantification of uncertainties for reliable reserve estimation (De Lucia et al. 2011).

Correlation length defines the spatial correlation that exists between pore spaces in porous media which provide details of correlated reservoir heterogeneity for quantitative analyses (Bijeljic et al. 2013; Babaei and Joekar-Niasar 2016). In addition, the importance of correlation length for multiphase fluid flow simulation was demonstrated by Kalia and Balakotaiah (2009) in their study. Also, correlation length was incorporated into pore network models to describe correlated reservoir heterogeneity impact on two-phase flows (Knackstedt et al. 2001; Leng 2013; Babaei and Joekar-Niasar 2016). Araktingi

and Orr (1993) also reported that, permeability field distribution and correlation length have a significant effect on the fingering pattern in porous media. Johnson (1956) also pointed out that reservoir heterogeneity has a strong negative impact on oil recovery. It is also important to note that, most petroleum porous media used for reservoir modeling lack heterogeneity, thereby preventing capturing of real subsurface instabilities (Islam et al. 2010). Craig (1971) noticed that the existence of fingering as a subsurface instability on different length scales in petroleum reservoirs appears to be one of the unresolved challenges in the petroleum industry. One enhanced oil recovery (EOR) method of great potential in overcoming water mobility is through polymer flooding (Daripa et al. 1988; Delamaide 2014) which increases injected fluid viscosity by preventing viscous fingering. Despite the reliability of polymer flooding in improving sweep efficiency, its performance still requires optimization for flow stability, but not treated in this work.

Nevertheless, the generation of these stochastic porous media realizations require high-resolution schemes, not to misinterpret numerical dispersion as subsurface geological features inherent in porous media. According to Zhang and Al Kobaisi (2017), despite many years of intensive investigation into simultaneous flow of water and oil in petroleum reservoirs, yet, it still poses serious challenges for reliable and accurate numerical reservoir simulation. Meanwhile, thorough investigation of the weakness of commonly used upstream mobility weighting schemes in conventional black oil simulators oftentimes result into substantial amount of spurious oscillations and unphysical solutions (Taggart and Pinczewski 1985). Even, properly constrained two-point upstream weighting scheme proposed as an alternative method is not monotonicity-preserving (Rubin and Blunt 1991) and such a limitation has also motivated the present work. Furthermore, higher order differencing schemes (central differencing scheme (CD), quadratic upstream interpolation for convective kinematics (QUICK), etc.) have been developed and implemented for discretizing convective terms in multiphase fluid flow simulation. But then, the implementation of boundary conditions, over and undershoot in numerical solutions are a source of concern for high-order schemes which led to the development of second-order TVD schemes to obtain oscillation-free solutions of higher order schemes (Versteeg and Malalasekera 2007). The insight gathered from these studies is that, the implementation of high-resolution second-order schemes into fully implicit method (FIM) conventional simulators to capture and characterize subsurface fluid flow dynamics and transport is a challenge in reservoir modeling (Rubin and Blunt 1991; Marcu 2004).

In view of the above developments, the first objective of this paper involves finite volume (FV) stochastic simulation

using Dykstra–Parson coefficient and autocorrelation lengths to generate 2D plausible stochastic permeability field values which were also used to generate porosity fields through a linear interpolation technique based on Carman–Kozeny equation. The proposed method was compared to other well-known methods of generating permeability fields, such as TBM and USRM which are scarcely used for fluid flow simulation. The second objective of this work is to apply some robust and powerful high-resolution schemes to attenuate large wiggles in low order schemes to capture accurately immiscible fluid flow subsurface details. In this study, SUPERBEE flux limiter (Roe 1985), MUSCL scheme (Van Leer 1979) and WENO scheme (Liu et al. 1994) were tested on a one-dimensional waterflood. Also, a validation test with classical BL analytical solution (Buckley and Leverett 1942) to detect overshoot and undershoot in numerical solutions was conducted.

Third, a comparative analysis was carried out between two-phase flow linearization schemes (simultaneous solution, SEQ and iterative IMPES) to find the most efficient and stable scheme with regards to ill-conditioning of the Jacobian matrix that may arise. However, Newton–Raphson method is the most commonly used algorithm for solving coupled nonlinear system of equations (Monteagudo and Firoozabadi 2007a, b). But, computational cost and memory requirement become expensive when the immiscible displacement problem is very large with restrictions. Byer (2000) stated in his study that, precondition approaches can be employed to simulate petroleum reservoirs by increasing the convergence rate of the Newton-type techniques. Another technique to improve this convergence rate is to apply regularization step under additional constraints on the discretization parameters (Radu et al. 2006), and automatic differentiation also speed up the Newton method. The problem associated with the Newton–Raphson method (NRM) is that, it is quadratic with local convergence rate. This notwithstanding, NRM also strongly depends on the initial estimate (List and Radu 2016) as well as computation of derivatives have motivated this study to test other linearization schemes.

Therefore, the system of nonlinear time-dependent partial differential equations were solved numerically (temporal and spatial discretization) using FIM (unconditional stable, large timestep size), iterative IMPES (conditionally stable, less computational cost and memory requirement with smaller timestep size) which is more stable than classical IMPES (Chen 2007; Kou and Sun 2010), and sequential solution method (MacDonald 1970) (solving pressure and saturation implicitly but not simultaneously in two conservative steps) were applied to solve the basic fluid flow equations. It is important to mention that both iterative IMPES and SEQ methods are easier to implement computationally (Pacheco et al. 2016). The significance of

correlation lengths on immiscible fluid flow transport in correlated stochastic porous media were also explored in this study. In summary, this study will serve as an indispensable tool in understanding spatial heterogeneity and the formulation of stabilized mobility control schemes to enhance better volumetric sweep efficiency in porous media.

This paper is structured into the following five sections. “**Methodology**” in section describes the physical model formulation, generation of permeability and porosity fields with illustrative examples using the proposed method, TBM and USRM techniques. The mathematical model and high-resolution schemes for oil and water fluid flow transport governing equations were formulated. “**Computer model development**” in section talks about the computer model development workflow and implementation strategy for reservoir description. Then, “**Numerical results and discussion**” in section dwells on numerical examples, results and discussion. Finally, “**Conclusions**” in section states key major conclusions drawn from the study.

Methodology

Physical model description

The 2D horizontal plane model consists of water injected at the left boundary with the right boundary producing water and oil (Fig. 1) similar to a direct line drive. In the reservoir physical model, the domain was initially saturated with oil without water saturation. The injector and producer horizontal wells were both perforated along the whole width of the structured computational model for linear flow pattern. The reservoir length is principal to flow direction and the reservoir width direction is perpendicular to flow direction. The side walls of the porous medium in Fig. 1 are impermeable to fluid flow. The rock and fluid properties used are summarized in Table 1 for the numerical experiments. The model consists of $100 \times 100 \times 1$ cell volumes with cell faces and cell centers discretized by finite volume method (FVM) which is mass conservative.

Stochastic modeling techniques for porous media architecture

The following procedures below were used to generate the 2D stochastic correlated permeability (dynamic property) field realizations, whereas these permeability field values were in turn used to generate 2D porosity field spatial variability (volumetric property) through a linear interpolation technique based on Carman–Kozeny equation. The proposed method of permeability field images generated were based on the idea of signal processing methodology to create random Gaussian field models. In addition, the

Fig. 1 2D Geometry of the discretized reservoir model ($100 \times 100 \times 1$ gridblocks)

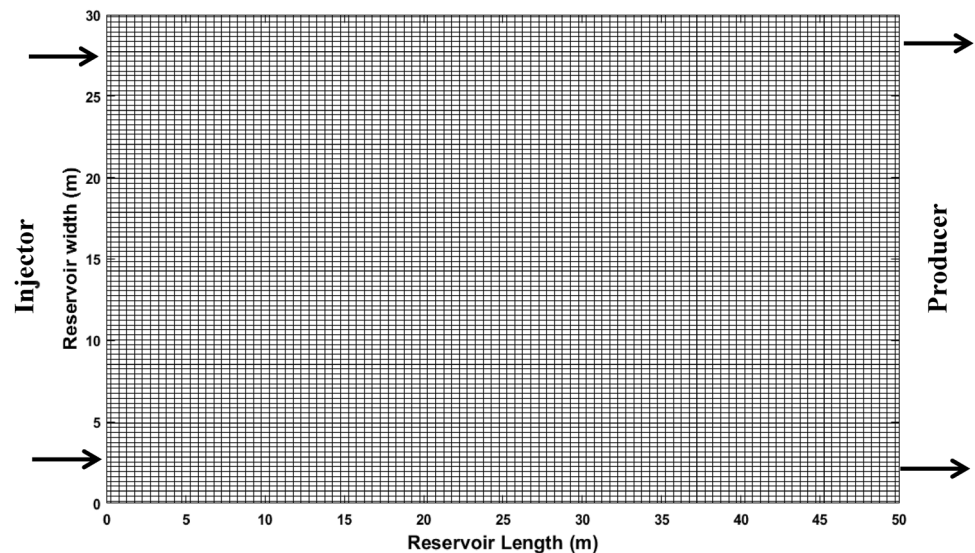


Table 1 Numerical model validation data

Reservoir parameters	Data values	English units
Oil viscosity (μ_o)	10×10^{-3}	Pa.s
Water viscosity (μ_w)	1×10^{-3}	Pa.s
Number of cell volume (N_x)	100	
Number of cell volume (N_y)	100	
Reservoir length (L_x)	50	m
Reservoir width (L_y)	30	m
Reservoir initial pressure (P_i)	1×10^5	Pa
Well injection pressure (P_{inj})	2×10^5	Pa
Water saturation (S_w)	0	Fraction
Oil saturation (S_o)	1	Fraction
Average porosity (ϕ)	0.20	Fraction
Average permeability ($K_{average}$)	2×10^{-12}	m^2
Correlation length (λ_x)	0.0–0.05	m
Correlation length (λ_y)	0.0–0.05	m
End point oil relative permeability (K_{ro})	1	
End point water relative permeability (K_{rw})	1	
Corey water exponent (n_w)	2	
Corey water exponent (n_o)	2	
Pressure accuracy	0.0001	
Saturation accuracy	0.0001	
Dykstra–Parsons coefficient (V_{DP})	0.0–0.9	

proposed method spelt out here is compared to widely known TBM and USRM for analyzing permeability maps and fluid flow simulations through them.

Methodology of the proposed permeability field

1. Rectangular grid mesh tessellation of the petrophysical properties (permeability and porosity fields) were created as shown in Fig. 1.

2. Dykstra and Parsons (1950) coefficient (V_{DP}) is the most common static measure of permeability variation as expressed in Eq. (1) which was used for perturbation. When $V_{DP} = 0$, then the reservoir is homogeneous, while $V_{DP} = 1$, the reservoir is highly heterogeneous.

$$V_{DP} = \frac{\log \bar{k} - \log k\sigma}{\log \bar{k}} = \frac{\text{standard deviation of } \text{Log}(k)}{\text{Average of } \text{Log}(k)}, \tag{1}$$

where \bar{k} is the median permeability or permeability value with 50 percent probability and $k\sigma$ is the permeability at 84.1 percent of the cumulative sample and σ is the standard deviation.

3. However, from the definition of V_{DP} (variance of the log-normal permeability distribution) in Eq. (1), an estimator relationship between V_{DP} and sample standard deviation (σ) of $\text{Log}(k)$ is rearranged as defined in Eq. (2) as:

$$\sigma = -\log(1 - V_{DP}). \tag{2}$$

4. Then, sample mean (μ) for log-normal randomly distributed field was estimated as written in Eq. (3) as:

$$\text{Log}(k_{\text{average}}) = \mu + 1/2\sigma^2, \tag{3}$$

where k_{average} is the average permeability.

5. The uncorrelated Gaussian random permeability field distribution (which amounts to adding a white noise to the simulated random field) was generated by using Eq. (4), but this noise needed to be filtered out by convolution with Gaussian kernel:

$$R = \sigma \cdot \text{randn}(N_x, N_y), \tag{4}$$

where R is the uncorrelated Gaussian random function distribution, N_x and N_y are the number of cells in x and y direction, respectively, randn function for generating random numbers drawn from a normal distribution.

6. With the obtained standard deviation [Eq. (2)] and a known average permeability, the Gaussian log-normal uncorrelated permeability field distribution generated from step 5 with white noise was pass through a Gaussian filter (smooth dataset). In two dimensions (x, y), the mathematical expression for the product of two Gaussian functions for the Gaussian filter impulse response (Gaussian surface) is given by Eq. (5) (Haddad and Akansu 1991; Mark et al. 2008) as:

$$\text{GF}(x, y) = \frac{1}{2\pi\sigma^2} \times e^{-\left(\frac{x^2+y^2}{2\sigma^2}\right)}, \tag{5}$$

where GF is the gaussian filter in two dimensions, x and y define the distance from the origin in the horizontal and vertical axis.

7. A convolution (faltung) with Gaussian filtering algorithm was used to achieve a correlated hydraulic conductivity field from the uncorrelated hydraulic conductivity field generated in step 5. This convolution was efficiently performed using Matlab (2016) discrete 2D fast Fourier transform (FFT) [Eq. (6)], and 2D inverse fast Fourier transform (IFFT) [Eq. (7)] as well as normalization of prefactors:

$$Y_{k+1,j+1} = \sum_{p=0}^{a-1} \sum_{q=0}^{b-1} \omega_a^{pk} \omega_b^{qj} X_{p+1,q+1}, \tag{6}$$

ω_a and ω_b are complex roots of unity, $\omega_a = e^{-2\pi i/a}$, $\omega_b = e^{-2\pi i/b}$, where a -by- b is matrix, i is the imaginary unit, k and p are indices that run from 0 to $a - 1$, j and q are indexes that run from 0 to $b - 1$.

$$X_{k,j} = \frac{1}{a} \sum_{p=1}^a \frac{1}{b} \sum_{q=1}^b \omega_a^{pk} \omega_b^{qj} Y_{p,q}, \tag{7}$$

ω_a and ω_b are complex roots of unity, $\omega_a = e^{2\pi i/a}$, $\omega_b = e^{2\pi i/b}$, where k runs from 1 to a , and j runs from 1 to b .

8. The results of R in step 5 and the Gaussian filter (GF) in step 6 are transformed and evaluated by 2D FFT and the results are multiplied as indicated in Eq. (8). The FFT transformation is back transformed using 2D IFFT to obtain convoluted Gaussian correlated field. In furtherance, the correlated surface generated with convolution, 2D FFT, 2D IFFT and normalization of prefactors through another filter is expressed in Eq. (8) (Bergström 2012). However, according to Garcia and Stoll (1984), proper care must be taken in choosing appropriate prefactors during IFFT (FFT back transformation) to ensure satisfied relations of spatially correlated Gaussian random fields.

$$f = \frac{2}{\sqrt{\pi}} \times \left[\frac{L_x}{\sqrt{N_x \times N_y}} \right] \times X_{k,j} \left[Y_{k+1,j+1}(R) \times Y_{k+1,j+1}(F) \right], \tag{8}$$

where L_x is the length of computational domain, λ_x and λ_y represents autocorrelation lengths in both x and y directions, respectively.

9. The correlation lengths (λ_x and λ_y) in Eq. (8) represent the maximum distance at which two points display a correlation used in generating the spatial variability of the geological media. If one autocorrelation length is used, then the medium is termed homogeneous. The final permeability field is generated by computing the

summation of sample mean [Eq. (3)] and the real part of Eq. (8) raised to an exponent ($K = e^{[\mu + \text{real}(f)]}$) (Eftekhari and Schüller 2015).

10. The porosity field through a linear interpolation scheme is generated based on the permeability field values created using Dykstra–Parsons coefficient and autocorrelation lengths by employing Carman–Kozeny relation expressed in Eq. (9) (Lie 2014) as:

$$K = \frac{1}{8\tau A_v^2} \frac{\phi^3}{(1 - \phi)^2}, \quad (9)$$

where ϕ is the porosity which is a function of permeability, τ is tortuosity, A_v is the specific surface area.

Uniform sampling randomization method

USRM was used to generate homogeneous random permeability field compared to our proposed method and for fluid flow simulation. However, the uniform sampling variant of the randomization is made up of superposition of independent (Gaussian random variables of mean zero and unit variance) random sine modes (Radu et al. 2011). In this method (second-order homogeneous), isotropic correlation description is given by a function consisting of Euclidian norm and correlation length. This randomization method also exhibits good ergodic properties during simulation process of generating log-hydraulic conductivity field realizations. However, details about the mathematical implementation of this algorithm over a uniform grid can be found in Sabelfeld (1991) and Radu et al. (2011).

Turning bands simulation method

TBM is one of the earliest multidimensional random number generator simulation method used to generate spatially correlated permeability fields with its accuracy depending on the number of lines used. Whenever insufficient number of lines are used, it results into striping (artifact banding) in the simulated map (Emery and Lantuéjoul 2006). TBM performs simulation along unidimensional lines instead of synthesizing the multidimensional field directly with computational efficiency over a space domain and more efficient than LU decomposition algorithm (Gotway and Rutherford 1994). A non-conditional realization can be generated for visual inspections. The detailed and comprehensive mathematical algorithm of TBM for Gaussian random fields implemented in this study can be found in (Matheron 1973; Mantoglou and Wilson 1982; Emery and Lantuéjoul 2006).

Mathematical modeling

Mathematical model basic assumptions

1. Immiscible fluids and rock properties are incompressible.
2. The solid matrix is non-deformable
3. Molecular diffusion, surface tension and capillary pressure were ignored.
4. The fluids are Newtonian and gravitational force is ignored.
5. Chemical reactions are not included and no phases change.
6. Viscous forces dominate, and capillary effects were neglected.

Immiscible two-phase flow transport in porous media

Applying macroscopic Darcy law as a momentum transport equation for saturated flow of oil and water in porous media for each control volume (CV) is written in Eq. (10) as:

$$\vec{u}_\alpha = -\frac{kk_{r\alpha}}{\mu_\alpha} \nabla p_\alpha, \quad (10)$$

where \vec{u} is the velocity vector, $k_{r\alpha}$ is the relative permeability of a phase, k is absolute permeability tensor, μ is the viscosity of fluid, p is the reservoir pressure, ∇ is the gradient operator, α is the oil and water phase. Total fluid mobility is the summation (λ_T) of water phase mobility (λ_w) and oil phase mobility (λ_o) as defined in Eq. (11) as:

$$\lambda_T = k(x) \left[\frac{k_{rw}(S_w(x, t))}{\mu_w} + \frac{k_{ro}(S_o(x, t))}{\mu_o} \right], \quad (11)$$

where $S_w(x, t)$ and $S_o(x, t)$ are saturation of water and oil phase, respectively, defined in space and time. A displacement stability criterion for unstable flow is when mobility ratio is greater than one (upstream mobility greater than downstream mobility), and vice versa. The total Darcy velocity (u_T) is the summation of water and oil velocities given in Eq. (12) as:

$$u_T = -\lambda_T \nabla p. \quad (12)$$

Therefore, for an incompressible fluid flow, the continuity equation is read by Eq. (13) as:

$$\nabla \cdot u_T = 0. \quad (13)$$

Substituting Eqs. (11) and (12) into Eq. (13) leads to Eq. (14) as:

$$\nabla \cdot \left[-k \left(\frac{k_{rw}(S_w)}{\mu_w} + \frac{k_{ro}(S_w)}{\mu_o} \right) \nabla p \right] = 0. \quad (14)$$

Linearizing Eq. (14) using Taylor series expansion resulted into Eq. (15) as:

$$\begin{aligned} & \nabla \cdot \left[-k \left(\frac{k_{rw}(S_{wi})}{\mu_w} + \frac{k_{ro}(S_{wi})}{\mu_o} \right) \nabla p \right] \\ & + \nabla \cdot \left[k \left(\frac{\partial k_{rw}(S_{wi})}{\mu_w \partial S_w} + \frac{\partial k_{ro}(S_{wi})}{\mu_o \partial S_w} \right) \nabla p_i S_w \right] \\ & = \nabla \cdot \left[k \left(\frac{\partial k_{rw}(S_{wi})}{\mu_w \partial S_w} + \frac{\partial k_{ro}(S_{wi})}{\mu_o \partial S_w} \right) \nabla p_i S_{wi} \right], \end{aligned} \quad (15)$$

where S_{wi} is the initial water saturation, S_w is the new values of water saturation, p_i is the initial reservoir pressure, k is the absolute permeability, k_{ro} and k_{rw} are relative permeability of oil and water, respectively. The relative permeability function in Eq. (15) for immiscible fluid flow transport was modeled using Corey (1954) correlation illustrated in Eqs. (16) and (17) for oil and water, respectively as:

$$k_{ro} = \left[\frac{1 - S_o}{1 - S_{wi}} \right]^{n_o} \left[1 - \left(\frac{S_o - S_{wi}}{1 - S_{wi}} \right) \right]^{n_o}, \quad (16)$$

$$k_{rw} = \left[\left(\frac{S_w - S_{wi}}{1 - S_{wi}} \right) \right]^{n_w}, \quad (17)$$

where S_{wi} is the initial water saturation, n_o is the Corey constant parameter for oil, n_w is the Corey constant parameter for water. The nonlinear flow equation in Eq. (15) for pressure gradient field has the following discretization terms in Eq. (18) as:

$$\begin{aligned} & - \text{Diffusion term} \left[k \left(\frac{k_{rw}(S_{wi})}{\mu_w} + \frac{k_{ro}(S_{wi})}{\mu_o} \right), p \right] \\ & + \text{Convection term} \left[u \left(\frac{k_{rw}(S_{wi})}{\mu_w} + \frac{k_{ro}(S_{wi})}{\mu_o} \right), p \right] \\ & = \text{Divergence term} \left[k \left(\frac{k_{rw}(S_{wi})}{\mu_w} + \frac{k_{ro}(S_{wi})}{\mu_o} \right), \nabla p_i \right] \end{aligned} \quad (18)$$

Whenever the pressure gradient is known from Eq. (18), then water velocity from Eq. (12) can be estimated to be used in the water transport Eq. (19). For simultaneous oil and water flow transport in a stochastic porous medium, the conservation equation of the water transport is specified in Eq. (19) as hyperbolic saturation equation:

$$\phi \frac{\partial S_w}{\partial t} + \nabla \cdot \left(- \frac{k k_{rw}(S_w)}{\mu_w} \nabla p \right) = 0. \quad (19)$$

Again, linearizing Eq. (19) using Taylor series expansion for a function of two independent variables yielded Eq. (20) as:

$$\begin{aligned} & \phi \frac{\partial S_w}{\partial t} + \nabla \cdot \left(- \frac{k k_{rw}(S_{wi})}{\mu_w} \nabla p \right) \\ & + \nabla \cdot \left(- \frac{k}{\mu_w} \frac{\partial k_{rw}(S_{wi})}{\partial S_w} \nabla p_i S_w \right) \\ & = \nabla \cdot \left(- \frac{k}{\mu_w} \frac{\partial k_{rw}(S_{wi})}{\partial S_w} \nabla p_i S_{wi} \right) \end{aligned} \quad (20)$$

But the total saturation of both oil and water flow in porous media is defined in Eq. (21) as:

$$S_o + S_w = 1. \quad (21)$$

The nonlinear water transport flow equation in Eq. (20) has the following discretization terms in Eq. (22) as:

$$\begin{aligned} & \text{Transient term} (\Delta t, S_w) \\ & - \text{Diffusion term} \left[\left(- \frac{k k_{rw}(S_{wi})}{\mu_w} \nabla p \right), S_w \right] + \\ & \text{Convection term} \left[u \left(- \frac{k}{\mu_w} \frac{\partial k_{rw}(S_{wi})}{\partial S_w} \nabla p_i \right), S_w \right] \\ & = \text{Divergence term} \left[\left(- \frac{k}{\mu_w} \frac{\partial k_{rw}(S_{wi})}{\partial S_w} \nabla p_i \right), S_{wi} \right]. \end{aligned} \quad (22)$$

With regards to discretization terms in Eqs. (20) and (22), these result into a system of coupled linear simultaneous equations expressed in Eq. (23). The primary unknowns in Eq. (23) are pressure and saturation for the simultaneous solution (SS) method (Douglas et al. 1959; Eftekhari and Schüller 2015):

$$\begin{aligned} & \begin{bmatrix} J_{pm} + M_{bcp} & J_{S_{wm}} \\ J_{pn} & J_{S_{wn}} + M_{bcSw} \end{bmatrix} \begin{bmatrix} P \\ S_w \end{bmatrix} \\ & = \begin{bmatrix} \text{RHS}_m + \text{RHS}_{bcp} \\ \text{RHS}_n + \text{RHS}_{bcSw} \end{bmatrix}, \end{aligned} \quad (23)$$

where J is the Jacobian matrix, m denotes the continuity equation for pressure while n indicates water saturation equation, M_{bc} terms denotes boundary conditions matrix terms for pressure and water saturation equations, P is pressure, S_w is water saturation, RHS indicates right-hand side of the coupled equations, RHS_{bc} term signifies right-hand side boundary conditions matrix terms for pressure and water saturation equations.

Solution technique to immiscible fluid flow in porous media transport

Newton–Raphson method (NRM) The method used to solve the system of linearized equations in Eq. (23) is Newton–Raphson powerful iterative method which is quadratic but only locally convergent with computation of derivatives (Bergamashi and Putti 1999). However, at every timestep, Eq. (23) needs to be solved in a loop until new values converge to initial values (Farnstrom and Ertekin 1987). This is because the convergence of the

Newton–Raphson algorithm is not guaranteed when the initial guess is not close enough to the solution, which implies a restriction on the timestep size (computational cost and memory requirement when problem size increases). The tractable iterative algorithm implemented in this study is solved concurrently and expressed in Eqs. (24) and (25), respectively as:

$$X_{k+1} = X_k - \frac{f(X_n)}{f'(X_n)}, \tag{24}$$

$$\begin{bmatrix} P^{n+1} \\ S_w^{n+1} \end{bmatrix} = \begin{bmatrix} P_o \\ S_{wo} \end{bmatrix} - \begin{bmatrix} \frac{\partial(J_{pm} + M_{bcp})}{\partial P} & \frac{\partial(J_{Swm})}{\partial S_w} \\ \frac{\partial(J_{pn})}{\partial P} & \frac{\partial(J_{Swn} + M_{bcSw})}{\partial S_w} \end{bmatrix}_{(P_o, S_{wo})}^{-1} \times \begin{bmatrix} (J_{pm} + M_{bcp})P_o + (J_{Sw1})S_{wo} - (RHS_m + RHS_{bcp}) \\ (J_{pn})P_o + (J_{Swn} + M_{bcSw})S_{wo} - (RHS_n + RHS_{bcSw}) \end{bmatrix}. \tag{25}$$

It is important to state here that the FIM Newton–Raphson iterative method for two-phase fluid flow in stochastic porous media was compared in terms of convergence rate and stability to iterative IMPES and SEQ linearization schemes. The details of these linearization schemes implemented in this study can be found in (Lacroix et al. 2003; Pacheco et al. 2016).

Methodology of high-resolution models for immiscible fluid flow transport

Here, it is the discretisation of the convective flux term that requires special attention to represent fluid flow patterns, since our goal is to find a scheme with a higher order of accuracy without wiggles for high-resolution (Harten 1983) shock-capture. Additionally, to estimate the average value of water saturation at cell faces over the mesh structure as shown in Fig. 1 based on velocity direction. Equation (19) describing incompressible fluid flow in porous media is rewritten in Eq. (26) as:

$$\phi \frac{\partial S_w}{\partial t} + \nabla \cdot (f_w u_T) = 0, \tag{26}$$

where $f(s_w) = \frac{z_w}{z_T}$ is the fractional flow of water.

The spatial domain (Fig. 1) is divided into finite volume cells (*i*th) and taking volume integral over the total volume of a cell (*v_i*) from Eq. (26) is expressed in Eq. (27) as:

$$\int_{v_i} \frac{\partial s}{\partial t} dv + \int_{v_i} \nabla \cdot f(s) dv = 0. \tag{27}$$

Also, the volume integrals in the partial differential equation in Eq. (27) contain a divergence term which is

converted into surface integrals by employing the divergence theorem given in Eq. (28) as:

$$\oint_v \nabla \cdot f dv = \oint_S f dS. \tag{28}$$

Integrating the first term in Eq. (27) yields volume average and applying divergence theorem in Eq. (28) to Eq. (27) second term results into Eq. (29) as:

$$v_i \frac{ds_i}{dt} + \oint_{S_i} f(s) \cdot n dS = 0, \tag{29}$$

where *n* is a unit vector normal to the surface and pointing outward, *S_i* denotes the total surface area of the cell.

The final general conservative result obtained in Eq. (30) is equivalent to Eq. (26) as:

$$\frac{ds_i}{dt} + \frac{1}{v_i} \oint_{S_i} f(s) \cdot n dS = 0 \tag{30}$$

The application of high-resolution scheme consists of adding a diffusive term to second-order Lax–Wendroff scheme (Wendroff 1960). Equation 31 describes incompressible flow of a linear convection equation in a one-dimensional porous media and assuming that the flow is from left to right which can be extended to two dimensions with the same flow properties. Therefore, the numerical approximations to scalar conservation hyperbolic equation by recalling Eq. (26) is given by:

$$\begin{aligned} \frac{\partial s}{\partial t} + \frac{\partial f(s)}{\partial x} &= 0, \\ s(x, 0) &= s_0(x), \end{aligned} \tag{31}$$

where the flux *f(s)* is a known function of *s* as the saturation of water phase.

The upwind differencing (transportiveness, conservativeness, boundedness and accurate) or ‘donor cell’ differencing scheme takes into account flow direction when determining cell face value. Applying first order upwind scheme to Eq. (31) leads to a numerical scheme written in a conservative form as Eq. (32) as:

$$s_i^{n+1} = s_i^n - \eta \left(\Delta s_{i-1/2}^{n+1} \right), \tag{32}$$

where *s_{iⁿ}* is the nodal values.

Meanwhile, the conservative form of Lax–Wendroff scheme for a nonlinear equation yields Eq. (33) as:

$$\begin{aligned} s_i^{n+1} = s_i^n - \frac{\eta}{2} \left(\Delta s_{i-1/2}^{n+1} + \Delta s_{i+1/2}^{n+1} \right) \\ + \frac{\eta^2}{2} \left(\Delta s_{i+1/2}^{n+1} - \Delta s_{i-1/2}^{n+1} \right), \end{aligned} \tag{33}$$

where upstream face/edge, $\Delta s_{i+1/2} = s_i - s_{i-1}$; downstream face/edge $\Delta s_{i-1/2} = s_i - s_{i-1}$ of the i th cell, courant number (mesh ratio) $\eta = \frac{\Delta t}{\Delta x}$

Therefore, reorganizing equation Eq. (33) results into Eq. (34) as:

$$s_i^{n+1} = s_i^n - \eta \Delta s_{i-1/2}^{n+1} - \frac{1}{2} \eta (1 - \eta) \left(\Delta s_{i+1/2}^{n+1} - \Delta s_{i-1/2}^{n+1} \right). \quad (34)$$

From Eq. (33) which represents Lax–Wendroff scheme amounts to adding an anti-diffusion flux to an upwind scheme. However, this anti-diffusion term makes Lax–Wendroff scheme second-order accurate, although it creates non-physical oscillations in the presence of shocks and discontinuity. TVD is a property that is used in the discretisation of equations governing multiphase fluid flow in porous media. Hence, high-order resolution schemes (SUPERBEE, WENO and MUSCL) were imposed to limit anti-diffusion flux to obtain second-order high-resolution scheme between fluxes of a high-order scheme and that of a low order scheme. Therefore, the flux limiter is a function of the ratio of two consecutive gradients applied to Eq. (34). This application resulted into Eq. (35) as TVD fluid flow equation:

$$s_i^{n+1} = s_i^n - \eta \Delta s_{i-1/2}^{n+1} - \frac{1}{2} \eta (1 - \eta) \left[\psi \left(r_{i+1/2}^{n+1} \right) \Delta s_{i+1/2}^{n+1} - \psi \left(r_{i-1/2}^{n+1} \right) \Delta s_{i-1/2}^{n+1} \right], \quad (35)$$

where ψ is the flux limiter function taken to be non-negative so as to maintain the sign of the anti-diffusive flux.

The ratio of the second-order term is also expressed in Eq. (36), where $\psi \left(r_{i+1/2}^{n+1} \right)$ is chosen so that it is approximately $\psi(1) = 1$ in smooth regions of the profile, giving accurate results. In regions where an unrestrained second-order contribution would produce oscillations (where the value of the second derivative is large), this term is allowed to vary in a manner which precisely eliminates their formation and $\left(r_{i+1/2}^{n+1} \right)$ is chosen to be a ratio of the successive second-order terms and a function of consecutive gradients.

$$\psi_{i+1/2}^{n+1} = \psi \left(r_{i+1/2}^{n+1} \right), r_{i+1/2}^{n+1} = \frac{\Delta s_{i-1/2}^{n+1}}{\Delta s_{i+1/2}^{n+1}} \quad (36)$$

According to Roe (1985), accurate solutions are obtained without spurious oscillations using TVD flux limiters that satisfies Sweby (1984) constraints. The computational codes developed in this work implements Sweby (1984) monotonicity-preserving sufficient conditions necessary for a scheme to be TVD in terms of the $r - \psi$ relationship. This implies that, they are designed to pass through TVD regions to guarantee stability of the scheme.

Thus, the requirement for second-order accuracy in terms of the relationship for linear upwind terms are as follows (Brantson et al. 2018):

1. If $0 < r < 1$ the upper limit is $\psi(r) = 2r$, for TVD schemes $\psi(r) \leq 2r$
2. If $r \geq 1$ the upper limit is $\psi(r) = 2r$, for TVD schemes $\psi(r) \leq 2r$
3. For the relationship in terms of $\psi = \psi(r)$, a second-order accurate scheme should pass through the point (1, 1) in the $r - \psi$ diagram.

The TVD flux limiter scheme applied to first order scheme sharp concavity profile changes is known by Roe (1985) as SUPERBEE applied to Eq. (35) expressed in Eq. (37) as:

$$\psi(r) = \max[0, \min(2r, 1), \min(r, 2)]; \lim_{r \rightarrow \infty} \psi(r) = 2 \quad (37)$$

The weighted essentially non-oscillatory (WENO) schemes can numerically approximate solutions of hyperbolic conservation laws and other convection dominated problems with high-order accuracy in smooth regions and essentially non-oscillatory transition for solution discontinuities. WENO construction (Eq. (38)) is an improvement on essentially non-oscillatory (ENO) applied to Eq. (35). Equation 38 describes the implementation of the scheme used in this study by Liu et al. (1994) as:

$$\psi(r) = \max[0, \min(r + b)], \quad (38)$$

The MUSCL scheme is also tested as a second-order TVD scheme to obtain spatial accuracy in the smooth parts of the numerical solution defined in Eq. (39) as applied to Eq. (35):

$$\psi(r) = \max[0, \min(2r, \min(0.5(1+r), 2))], \quad (39)$$

where $\psi(r)$ is the flux limiter function, b is the biasing parameter.

Monotonicity-preserving second-order schemes have the property that the total variation of the discrete solution should diminish with time. Hence, the term TVD. The total variation (TV) is stated in Eq. (40) for the hyperbolic advective term in Eq. (31) as:

$$\text{TV} = \int \frac{\partial f(s)}{\partial x} \partial x = 0. \quad (40)$$

The TV in saturation is non-increasing and the TV for a discrete case solution is defined in Eq. (41) as:

$$\text{TV}(s_i^{n+1}) = \sum_i |s_{i+1}^{n+1} - s_i^{n+1}|. \quad (41)$$

A numerical method at every timestep is said to be TVD, if Eq. (42) is satisfied as:

$$\text{TV}(s_i^{n+1}) \leq \text{TV}(s_i^n), \quad (42)$$

where n and $n + 1$ are previous and current timestep, respectively.

Initial and boundary conditions

To complete the formulation of the model, the initial and boundary conditions are required by imposing restrictive conditions. The following initial and boundary constraints were specified for the simultaneous two-phase flow in a stochastic porous media for the modeling process.

$S_o = 1; S_w = 0$, where S_o is saturation of oil and S_w is saturation of water.

For an advancement of pressure and saturation solution in time until final simulation is reached is given by:

$t = t_o + \Delta t$, where t is the new timestep, t_o is the initial timestep = 0, Δt is the timestep size.

The boundary conditions were specified for both inflow (left) and outflow (right) of the stochastic porous medium using ghost border cells approach. In this current study, Dirichlet pressure boundary was specified for the left (constant injection pressure) and right-hand side (constant pressure boundary) of the porous medium. While Dirichlet constant water saturation boundary condition was specified for the left-hand side (LHS) of the perforated porous medium. The lateral walls of the computational domain are impermeable with no flow boundary conditions.

Computer model development

The mathematical models obtained from the previous sections require high-speed digital computer for implementation due to the size of the Jacobian matrix. In this paper, the steps used to develop the computer model is shown in Fig. 15 (Appendix). In Fig. 15, the workflow consists of internal nonlinear solver loop and external time loop under different flow conditions.

Numerical results and discussion

This section presents results, discussion and implementation of stochastic porous media modeling approaches as well as the linearization schemes. All simulations were conducted on a standard laptop (Samsung NP8500GM notebook with an intel i5 processor and 16 GB RAM) in Matlab (2016) programming environment.

Numerical reservoir simulator validation

BL analytical displacement (ideal case) was used to validate the high-order resolution schemes (SUPERBEE,

WENO and MUSCL schemes) by considering one-dimensional linear (1 m) petroleum reservoir (40 gridblocks) in a homogeneous medium. This is because, BL is free from numerical dispersion. A comparative analysis was made between saturation distributions provided by the various schemes to check significant numerical dispersion (smearing) effect (Fig. 2) and the stability of the schemes. There was a good agreement of identical solution between the analytical solution, SUPERBEE, WENO and MUSCL schemes with lower numerical smearing than upwind scheme without no flux limiting scheme (ahead of other schemes) in capturing the shock front. This can be attributed to the fact that, despite upwind scheme being most stable and unconditionally bounded scheme, it gives false diffusion when transport properties are not aligned with gridlines and its low first order accuracy (Brantson et al. 2018). It is also important to state that, there was no over or undershoot in the numerical solutions confirming the robustness of the high-order resolution schemes for capturing fluid flow transport in porous media with acceptable level of numerical dispersion. It can clearly be seen from Fig. 2 that, Newton–Raphson method used converges despite being quadratic with a local convergence for a unidirectional flow. It is noteworthy to mention that the augmentation of grid cells (mesh resolution) will further reduce the level of numerical dispersion (Marcu 2004).

Numerical convergence criteria for the linearization schemes

The same one-dimensional model used as classical BL solution benchmark was solved by FIM method compared to

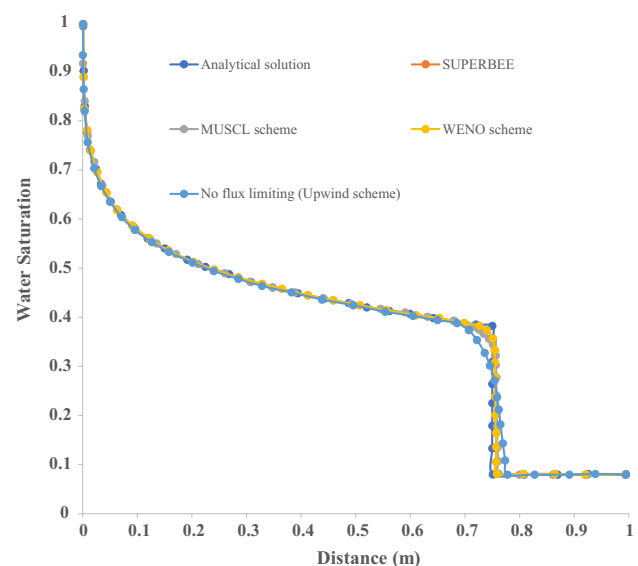


Fig. 2 Validation of the high resolution schemes with Buckley Leverett analytical solution (one dimensional water flood)

iterative IMPES and SEQ methods for numerical convergence rate analyses. These schemes were compared in terms of results accuracy, stability and computational time. The computation of residuals is the basic measure of a linearization scheme's solution convergence by quantifying the system of conserved equations errors in the solution field. The convergence rate of the solution is monitored by checking the water saturation residuals of the numerically solved governing equations as an indicator. Also, the minimum allowable saturation (difference between current iteration and last saturation iteration in any cell volume) and specified residual tolerance limit was set to 0.01 (Eftekhari and Schüller 2015) and 10^{-3} (Radu et al. 2015), respectively, before the start of the numerical simulation. Figure 3a shows a snapshot of the three linearization schemes tested in this study with their obtained water saturation residuals plot. It is also a known fact that any iterative numerical solution will never be exactly zero, but can be within an acceptable tolerance limit. Although the three linearization schemes were within the specified tolerance limit for capturing shock front. It can be observed from the residual monitors in Fig. 3a that, the three linearization schemes residuals reduce as simulation progresses. However, as the residuals decrease rapidly because of solution convergence, the water saturation residuals change less between iteration levels without any imbalance in the system. Furthermore, the lower the residual

value is, the more numerically accurate the solution for conserved quantities. It can be inferred from Fig. 3a that the saturation error estimates decrease as the number of iterations and timesteps increases. The linearization schemes residual monitors exhibit monotonic conserved convergence after about 200 iterations with stable numerical solutions. In addition, the residuals of SS method achieve more stability with lower residuals as compared to iterative IMPES and SEQ techniques. Similarly, the residuals drop and level off and become stable for each scheme. The SEQ method combines the advantage of SS and IMPES methods to attained stability and efficiency (Watts and Shaw 2005) as seen in Fig. 3a. But, it also has the problem of handling complicated capillary pressure curves which was ignored in our study. Numerical comparison of iterative IMPES, SS method and SEQ techniques for field scale numerical simulation of oil reservoirs for both saturated and undersaturated states were also performed by Chen et al. (2006). In summary, despite NRM being quadratic with local convergence, the numerical solutions were within acceptable tolerance limit.

Linearization schemes computational time

Another indicator test is the computational time taken by each linearization scheme for the 1D waterflood simulation. The three linearization schemes were tested on a unidirectional flow by recording the simulation CPU time. When the same number of grid nodes (100) were used for the same number of iterations (800), Fig. 3b indicates that the iterative IMPES scheme uses less CPU time (less costly method) in this study for simulating the fluid flow transport compared to SS and SEQ methods. This is then followed by SEQ method which also solves pressure and saturation equations implicitly, but in sequence, which reduces computational cost and memory (Chen et al. 2006) as seen in Fig. 3b. Lastly, SS method has larger system of equations with larger CPU time despite its stability and robustness (Fig. 3a). Therefore, it can be inferred that the SS required excessive computational cost and memory requirement. It can also be noticed from Fig. 3a, b that, CPU time will increase correspondingly as cell volumes increases for defined timestep.

Geostatistical simulation of permeability fields

This section compares the different stochastic methods for generating equiprobable permeability fields with different parametric setup in this study through geostatistical simulation. The plausible realizations have different petrophysical properties with different recovery factors when subjected to reservoir fluid flow simulation. Herein, the CPU simulation times for the geologic architectures were

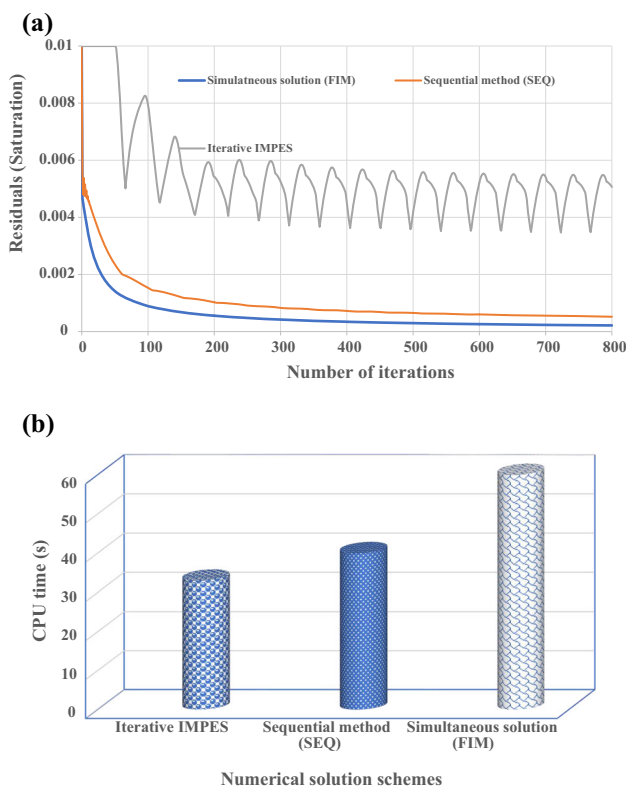


Fig. 3 a Residual monitors and rate of convergence plot b linearization schemes CPU time

also recorded for each realization generated on the rectangular grid mesh (Fig. 1). The colorbar in each figure give details about the ranges of permeability variations.

The proposed permeability map

In this part, plausible stochastic permeability field realizations were generated when correlation lengths were the same in both horizontal and vertical direction with different V_{DP} values. Figure 4a with V_{DP} of 0.2 indicates fairly homogeneous field, but when V_{DP} was increased to 0.5, the heterogeneity of the field increases as compared to Fig. 4a. In addition, Fig. 4c displayed a highly spatial heterogeneous field with V_{DP} of 0.8 unlike Fig. 4a, b for reservoir fluid flow simulation.

Uniform sampling randomization method permeability map

Three permeability map realizations were generated with uniform sampling randomization method (USRM) with statistically distributed samples of homogeneous fields. Figure 5a is highly permeable than Fig. 5b, c with Fig. 5c having slight heterogeneity in the random field. The uniform sampling variant of the uniform sampling randomization method is made up of superposition of random sine modes (Radu et al. 2011 and references therein). In the numerical simulation of the random field, exponential correlation exhibits good ergodic properties of the log-hydraulic conductivity field. All the realizations generated here are more homogeneous as compared to the realizations (Fig. 4) using our proposed method.

TBM permeability map

TBM is a highly efficient multidimensional simulation method that was used in this study to generate 2D equiprobable permeability field realizations through a series of one-dimensional simulation along lines with an exponential covariance model. Here, the model type that was implemented was exponential covariance model for stationary Gaussian random fields. From Fig. 6a, b, a visual impression and appreciation of artifact banding discontinuities occurred in the simulated maps when finite number of lines of 15 (Journal and Huijbregts 1978; Mantoglou and Wilson 1982) and 64 (Gneiting 1999) were used, respectively. This can be attributed to the fact that the lines were insufficient to generate the permeability maps. Hence, not ideal realizations for fluid flow simulation. But in Fig. 6c where the number of lines were increased to 1000 (Tompson et al. 1989; Freulon and de Fouquet 1991), no artifact banding/stripping occurred in the random field with improvement in the ergodic properties of the simulated

map. Emery and Lantuéjoul (2006) also obtained artifact banding with 15 lines, but with 1000 lines, the realization texture obtained improved with no perceptible artifacts as seen in our study (Fig. 6c). Comparatively, no artifacts were also observed in our proposed method and USRM. To validate the quality of the simulated permeability field (Fig. 6c) to be used for fluid flow simulation due to the problem of artifact banding beyond visual check. The simulated variogram was compared to the theoretical variogram algorithm plotted against distance when 1000 lines were used. It can be noticed from Fig. 6d that the average simulated statistics match the theoretical model almost perfectly.

CPU run-time for the simulated permeability maps

The three permeability map methods analyzed in this study CPU times were comparatively compared for the realizations generated. This is because, memory storage requirement becomes important when large number of random fields are to be generated with speed and accuracy. Figure 7 shows that USRM has the least CPU run-time in seconds followed by our proposed method and lastly the TBM technique, when a single realization was produced with each method. TBM has the highest CPU run-time due to CPU time devoted to post-processing the realization to be generated (Emery and Lantuéjoul 2006), but its simulation along lines is usually fast. In all, the three approaches achieved fast efficient simulation time at good computational cost.

Homogeneous immiscible displacement

Under homogeneous stable base case model for immiscible displacement scheme in this research, all rock (porosity and permeability values equal to the mean values) and fluid properties were kept constant (isotropic) in the computational domain. This implies horizontal permeability is equal to vertical permeability. Figure 8a shows non-perturbed field with no subsurface instability (flat interface) with stable recovery rate about 27% in 60 days. The plumes of unstable structures (Fig. 8b, c) were generated when a random distribution of permeability was introduced only at the inlet face (restricted to the ghost border cells near the injection well) of the porous medium at ($t = 0$ s), while the non-perturbed parts of the porous medium remain homogeneous. The merits of this method (spatial restriction to perturbation) of perturbing the initial saturation field was also applied by Riaz and Tchelepi (2006), Islam et al. (2010), Henderson et al. (2015), and Bouquet et al. (2017) in their studies for oil displacement in reservoirs. It can also be seen in Fig. 8b, c that, the oil displacement was piston-like, where oil in front of the shock was pushed out

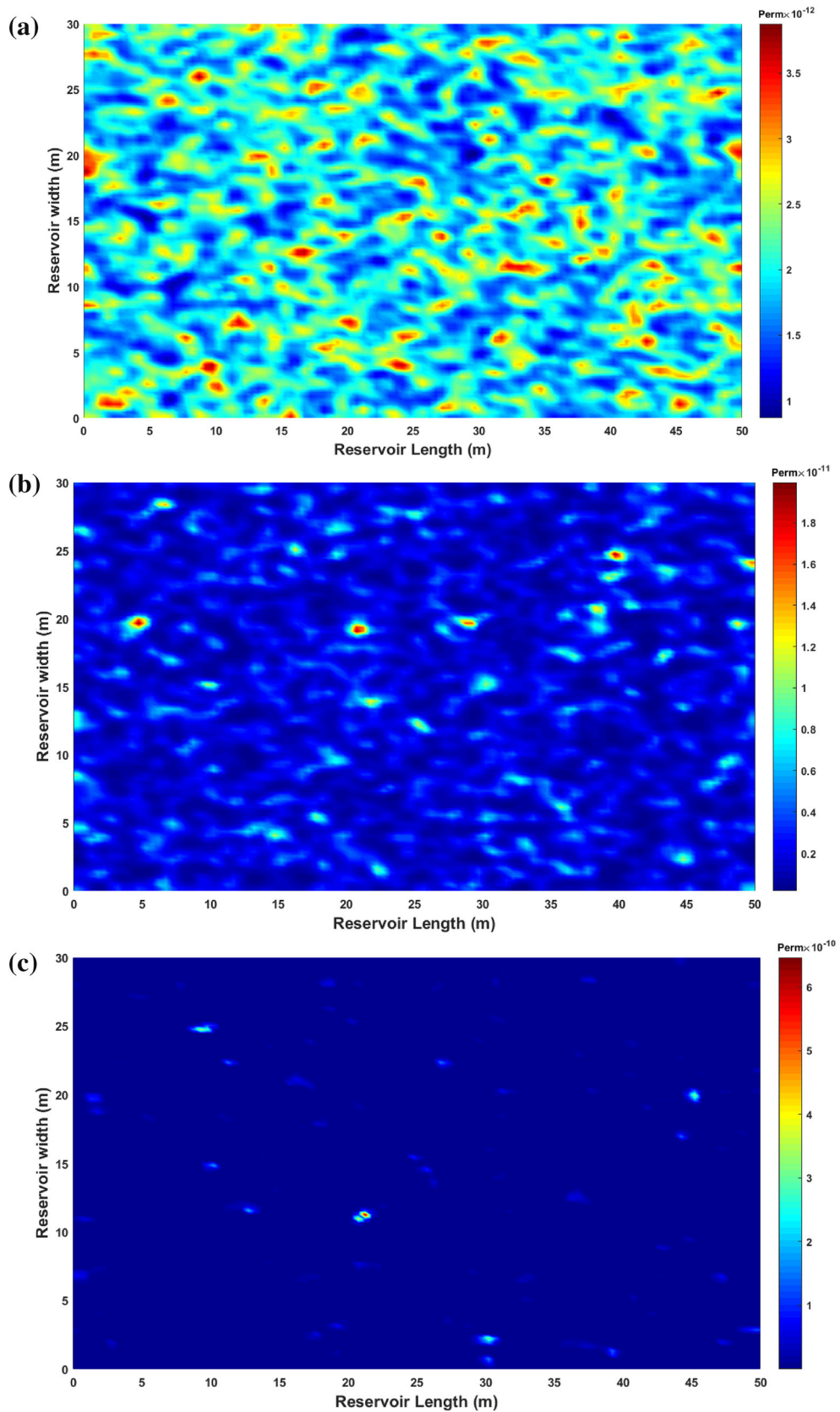


Fig. 4 Proposed permeability map **a** ($V_{DP} = 0.2$, $\lambda_x = 0.04$ m, $\lambda_y = 0.04$ m); **b** ($V_{DP} = 0.5$, $\lambda_x = 0.04$ m, $\lambda_y = 0.04$ m); **c** ($V_{DP} = 0.8$, $\lambda_x = 0.04$ m, $\lambda_y = 0.04$ m)

Fig. 5 Uniform sampling randomization simulation method permeability maps (**a**, **b** and **c**, $E(K) = 2 \times 10^{-12} \text{ m}^2$, $\sigma^2 = 0.130$, $\lambda_x = 1 \text{ m}$, $\lambda_y = 1 \text{ m}$)

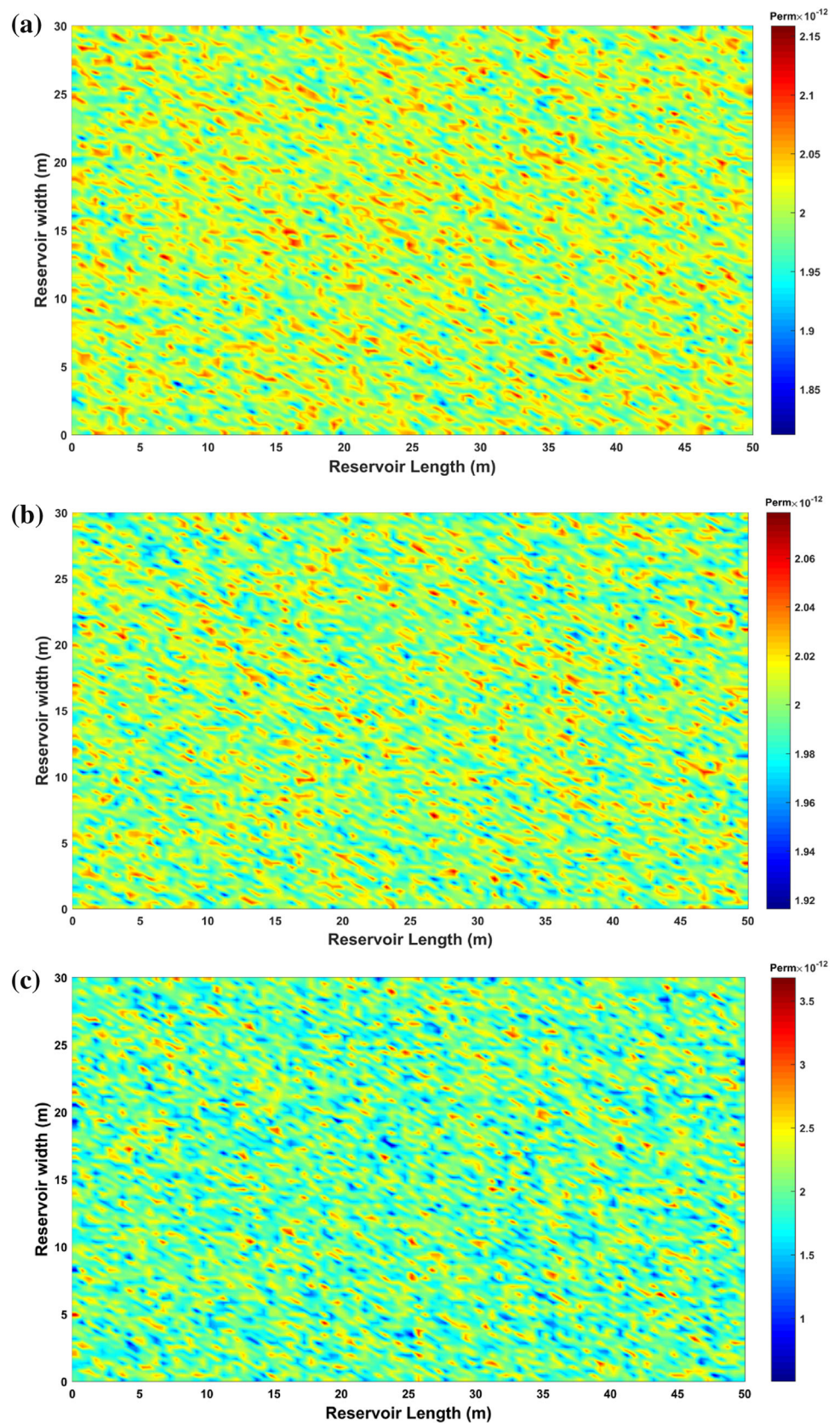
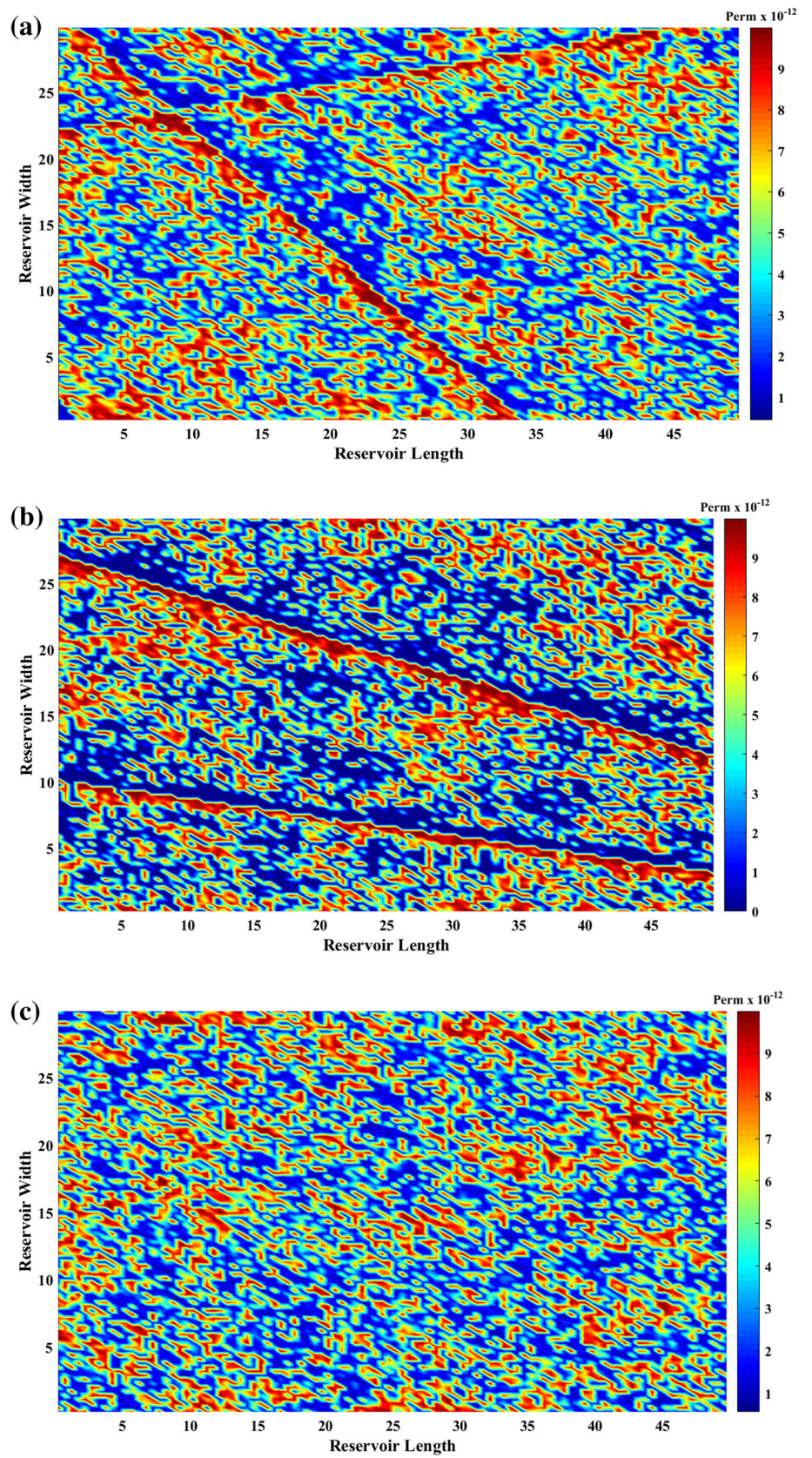


Fig. 6 TBM permeability map **a** 15 lines **b** 64 lines **c** 1000 lines



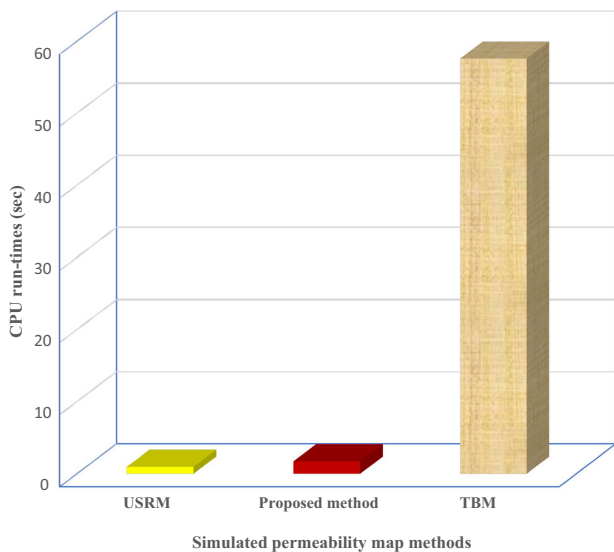


Fig. 7 CPU run-times for proposed method, TBM and USRM

of the domain having water behind shock with small subsurface instabilities. It can be detected from Fig. 8c that, instabilities initiated grow as oil was pushed out of the domain due to sufficient saturation fringe in the numerical simulation process (Bouquet et al. 2017). Eftekhari and Schüller (2015) also stated that V_{DP} of 0.01 which makes about 3% perturbation in a permeability field does not result into flow channeling, but can trigger viscous fingering initiations. The recovery factor for the piston-like quasi-homogeneous (Fig. 8c) displacement was approximately 24% in about 60 days as seen in Fig. 9, but less than Fig. 8a recovery factor due to fingering phenomenon.

Heterogeneous surface instabilities

Proposed method fluid flow simulation

This section dwells on heterogeneous permeability field fluid flow simulation through the three techniques used to generate the permeability fields. The porosity field is a function of permeability which was generated based on Carman–Kozeny relation as shown in Fig. 10. Figure 4a, c permeability realizations were used to simulate fluid flow through the stochastic field to observe subsurface instabilities. Figure 11a, b illustrate subsurface instabilities larger than the quasi-homogeneous base case (Fig. 8b, c). These instabilities were mainly characterized with tip splitting (bifurcation), spreading and coalescence of finger-like structures. However, these instabilities merge together as they are driven toward the wake of larger fingers because of the larger ones moving faster and preventing the growth of smaller ones. The specific spatial paths taken by the instabilities correspond to paths of local higher

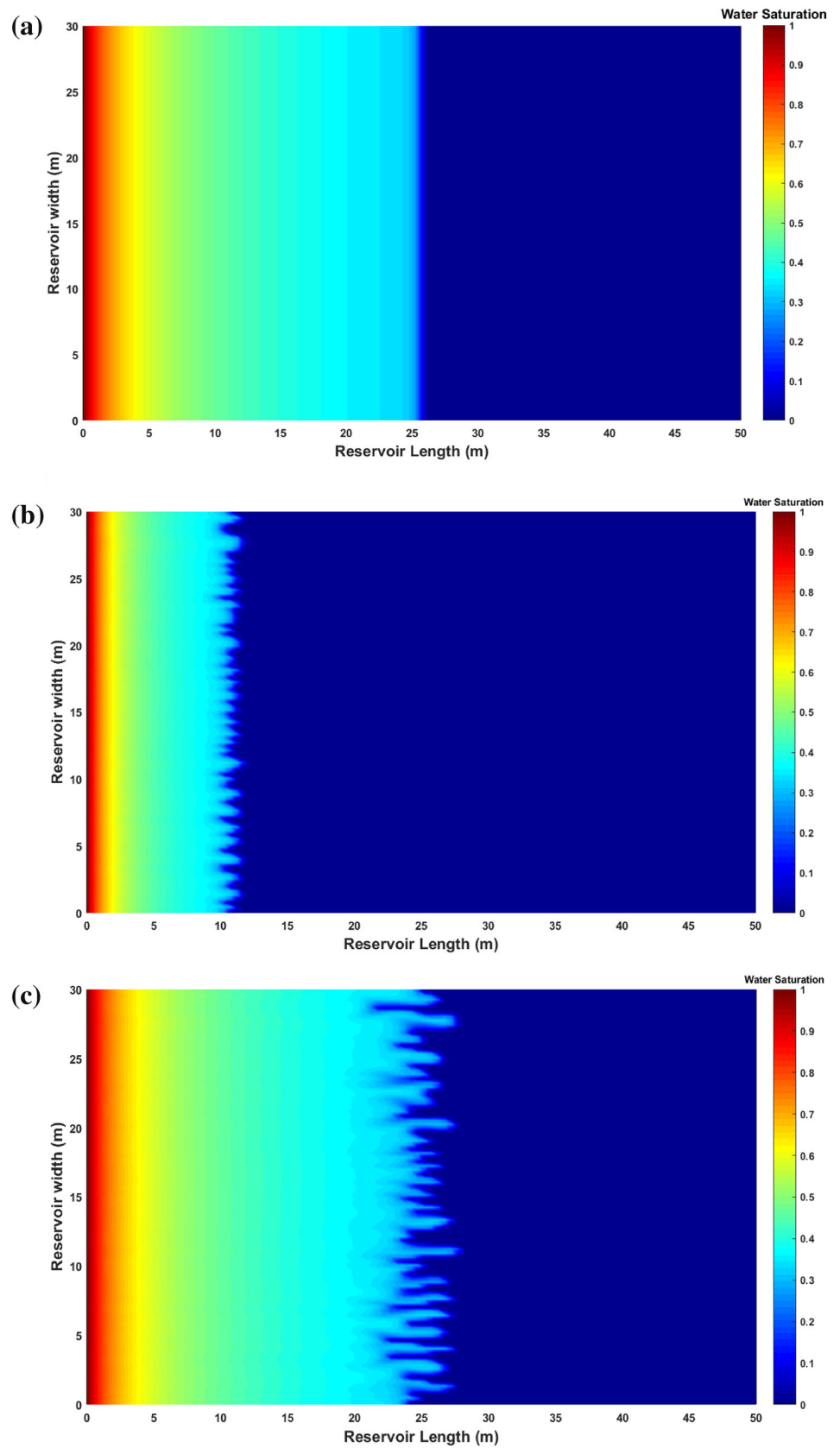
permeability zone. Hence, channeling phenomenon is susceptible in such high permeability zones (Doorwar and Mohanty 2016). Erandi et al. (2015) and Luo et al. (2017) also observed in their research that, fingering regime of a layer can be completely disrupted by modest levels of heterogeneity leading to channeling regime. Therefore, when Fig. 4a permeability field ($V_{DP} = 0.2$) was used for fluid flow simulation (Fig. 11a), the recovery factor was 23% in approximately 60 days. This recovery factor is almost close to Fig. 8c recovery factor of 24% denoting homogeneity for both cases, despite observation of fingering phenomenon. The displacement (Fig. 11a) is also piston-like with larger surface instabilities of viscous fingers due to weak perturbation with no significant impact of fingers' behavior.

On the other hand, the characterization of reservoir heterogeneity by permeability variation of most reservoirs falls within the range of 0.5–0.9 (Willhite 1986). Figure 11b shows a heterogeneous permeability map (Fig. 4c) with $V_{DP} = 0.8$. It can be inferred from Fig. 11b that, the subsurface instabilities were more severe as compared to when $V_{DP} = 0.0$ (Fig. 8a–c) and $V_{DP} = 0.2$ (Fig. 11a). Additionally, it can be noticed from Fig. 11b that, at the start of the simulation, the finger tips were more unstable and propagate further forward with the strong media heterogeneity causing the splitting phenomenon with continuous repetition till water breakthrough. This erratic behavior was observed as more mobile fingers ahead of their neighboring fingers outruns and shielded less mobile ones from further growth (Fig. 11b). Tip splitting and spreading pattern were also seen in (Fig. 11a, b) as pressure gradient is also larger near the tip of the finger causing the finger to split leading to different flow paths. The oil recovery factor due to subsurface instabilities can be seen in Fig. 9 when $V_{DP} = 0.8$ with 13% recovery rate in approximately 60 days. Therefore, the higher the permeability variation in porous media, the lesser the amount of oil recovered with increment in recovery time. Similarly, Fig. 11b depicts skeletal viscous fingers similar to Brownian trees of diffusion limited aggregation (DLA) formed possessing self-similarity nature of fractals (Zhang and Liu 1998).

Uniform sampling randomization method fluid flow simulation

In this part, the dynamic fluid flow simulation was simulated through Fig. 5c which was generated through USRM which has slight heterogeneity than Fig. 5a, b. The fingers behavior shown in Fig. 12 are similar to the homogeneous case demonstrated in Fig. 8c with unstable piston-like displacement characteristics. In Fig. 12, there is no bypass of oil unlike Fig. 11b due to permeability variation. The

Fig. 8 Homogeneous water saturation maps ($V_{DP} = 0.0$, $\lambda_x = 0.04$ m
(a) $t = 5.2261 \times 10^6$ s
(b) $t = 2.5398 \times 10^6$ s, (c)
 $t = 5.1877 \times 10^6$ s)



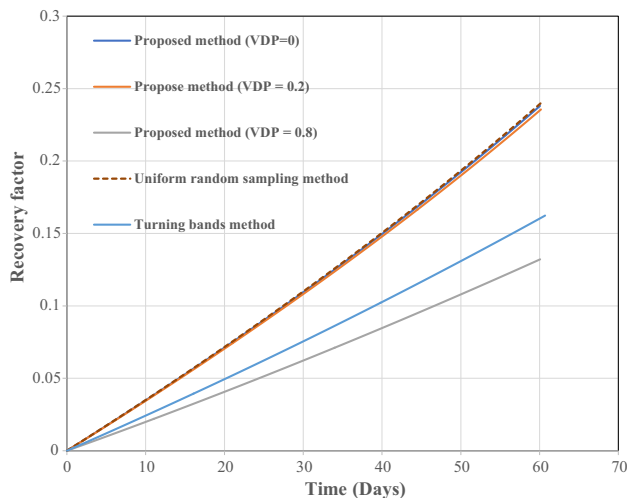


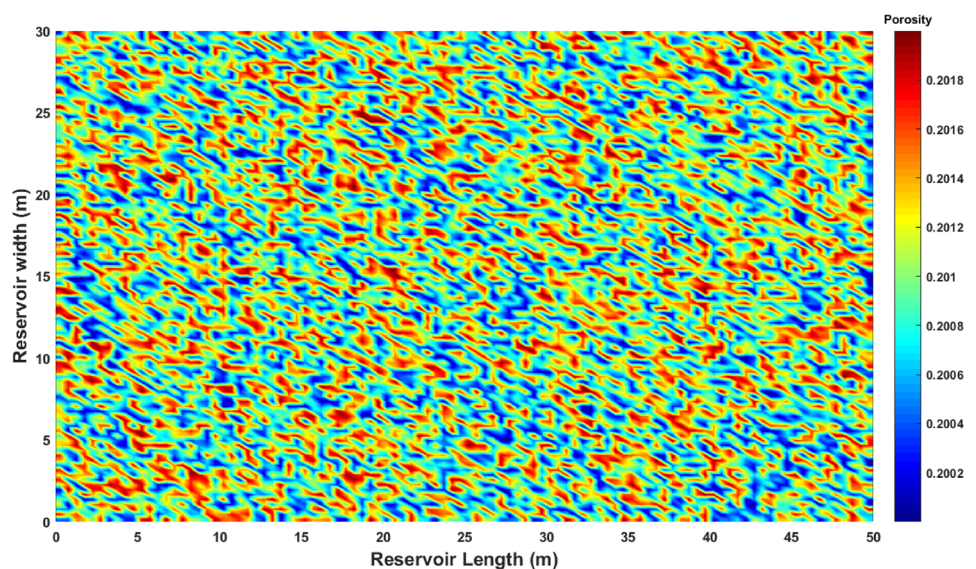
Fig. 9 Recovery factor for homogeneous and heterogeneous fields

obtained recovery rate for Fig. 12 is 24% in approximately 60 days in Fig. 9 similar to $V_{DP} = 0.0$ and $V_{DP} = 0.2$ which are indication of a more homogeneous system.

Turning bands method fluid flow simulation

Figure 6c TBM permeability field with good ergodic properties was employed for numerical simulation experiment to observe subsurface instabilities during water injection process. Furthermore, bypass of unswept regions were seen in Fig. 13 similar to Fig. 11b unlike Figs. 8a–c and 12 with no such phenomenon. Spreading and tip splitting were the dominant features seen on the water saturation map (Fig. 13). The recovery factor for Fig. 13 was 16% in 60 days as shown in Fig. 9 was higher than

Fig. 10 Porosity field realization



that of Fig. 11b due to higher permeability field values in Fig. 6c, but less than the recovery rate for Fig. 8c.

Water breakthrough time and the impact of correlation lengths on immiscible fluid flow distribution

Herein, correlated correlation lengths of 0.03 m (Fig. 14a) and 0.05 m (Fig. 14b) (below and above 0.04 m used in our analyses) same in both vertical and horizontal direction were employed with the proposed method to generate permeability realizations with V_{DP} of 0.5 to observe their impact on fluid flow simulation in subsurface. The various subsurface instabilities of spreading, shielding, merging, tip-splitting can clearly be visualized from both Fig. 14a, b with unswept regions coupled with unstable displacement. The sweep efficiency in Fig. 14a is better than in Fig. 14b with less residual oil saturation. One crucial observation noticed from both plots is that, there are islands of oil (bypass) surrounded by the invading fluid leading to breakthrough in both Fig. 14a, b. Inference drawn from Fig. 14b indicates that, increase in correlation lengths yielded more viscous fingers than in Fig. 14a. The oil recovered due to variation in correlation lengths for Fig. 14a and b are 32% and 27% when water breakthrough in 103 and 84 days, respectively, which had significant impact on fluid distribution in the stochastic media. The sensitivity of correlation lengths in reservoir fluid flow simulation should be considered when predicting future performance of petroleum reservoirs.

Fig. 11 Heterogeneous permeability field water saturation maps **a** ($V_{DP} = 0.2$, $t = 5.1985 \times 10^6$ s), **b** ($V_{DP} = 0.8$, $t = 5.1893 \times 10^6$ s)

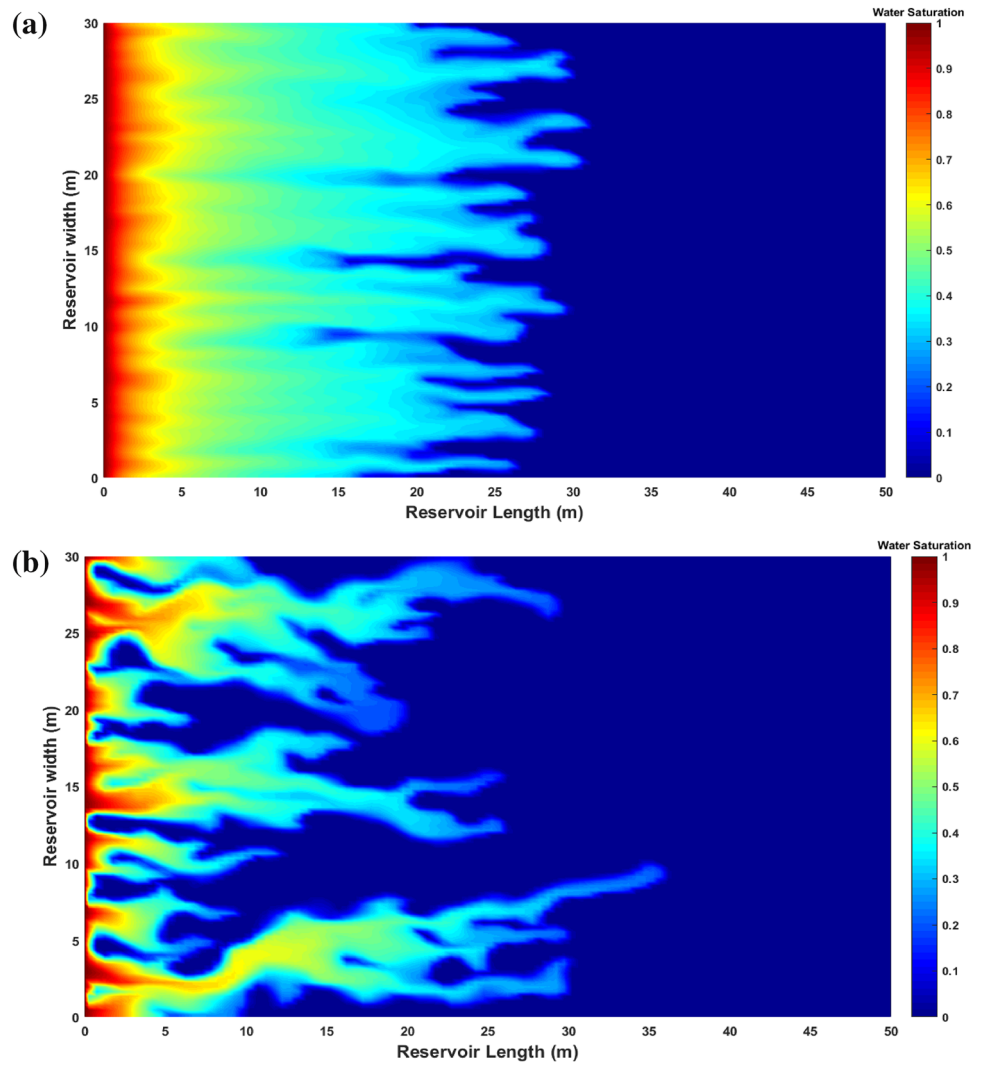


Fig. 12 Uniform sampling randomization method saturation field ($t = 5.1972 \times 10^6$ s)

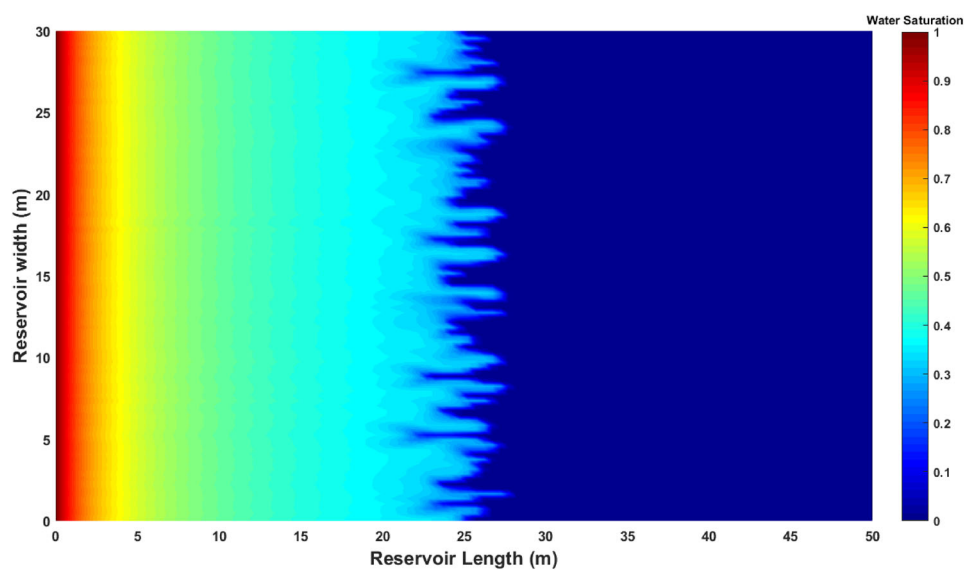


Fig. 13 Turning bands method water saturation map ($t = 5.1972 \times 10^6$ s)

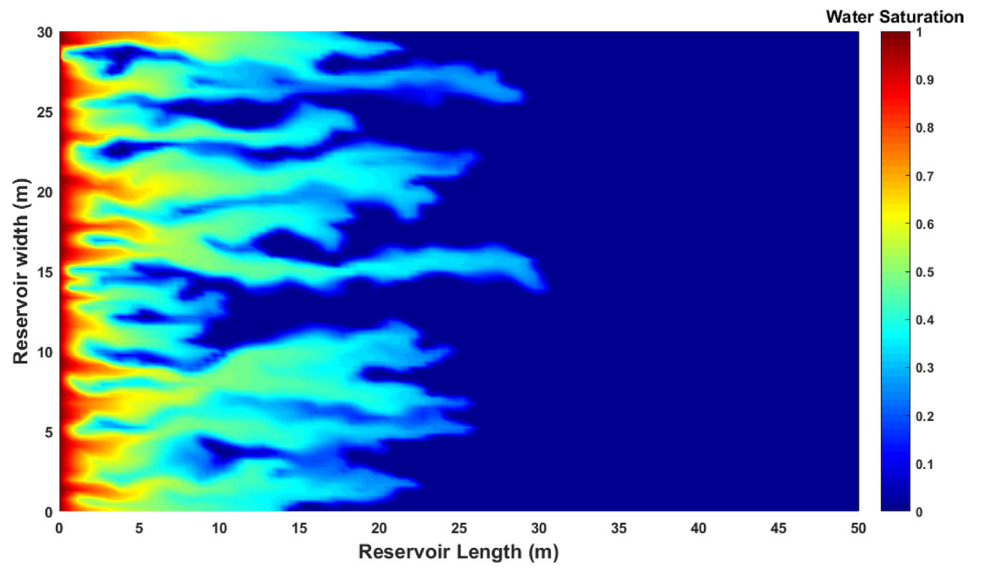
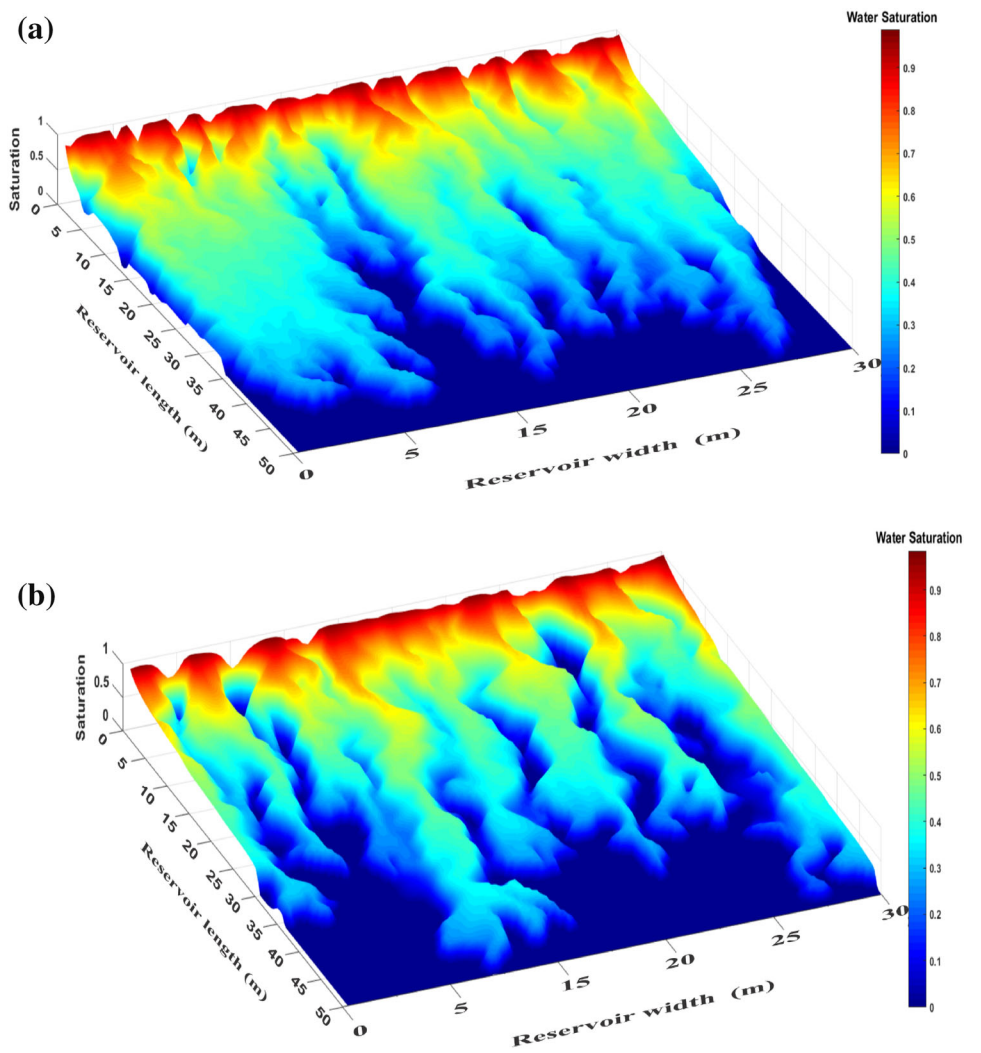


Fig. 14 Water saturation breakthrough time maps
a ($V_{DP} = 0.5$, $\lambda_x = 0.03$ m, $\lambda_y = 0.03$ m, $t = 7.233953 \times 10^6$ s),
b ($V_{DP} = 0.5$, $\lambda_x = 0.05$ m, $\lambda_y = 0.05$ m, $t = 8.823839 \times 10^6$ s)



Conclusions

In this present work, a two-dimensional numerical reservoir simulator developed was used to generate stochastic porous media for simulating subsurface instabilities during immiscible fluid flow displacement process. The following conclusions were made from the study:

- A proposed stochastic modeling approach for generating petroleum porous media (permeability and porosity fields) was incorporated into reservoir fluid flow simulation to improve production forecast in heterogeneous formations.
- The TBM and USRM techniques used for generating equiprobable spatial permeability fields were incorporated into reservoir fluid flow simulation. But banding artifacts were observed in the TBM permeability fields when finite number of lines were used.
- The linearization schemes of SS method, iterative IMPES and SEQ method were used for solving the two-phase problem without any non-physical solutions around shocks and discontinuities.
- High-resolution schemes of SUPERBEE flux limiter, WENO and MUSCL employed in the numerical simulator were monotonicity-preserving and fit well to the BL analytical solution with minimal smearing.
- A comparison was made between homogeneous and heterogeneous stochastic porous media in terms of recovery factor with less oil recovered in the heterogeneous formations due to interactions between heterogeneity and viscous fingering unlike the homogeneous formation media.
- Quantitative subsurface instabilities including shielding, coalescence, spreading, successive tip splitting,

channeling and skeletal fingers were observed on the permeability fields of the proposed method, TBM and USRM techniques.

- Finger widths which are often much smaller than typical reservoir simulation grid blocks were captured through numerical simulation.
- The effect of correlation lengths on immiscible fluid flow transport was investigated with larger correlation lengths yielding more significant viscous fingering effects.

Unit conversion

$$1 \text{ Darcy} = 9.86923 \times 10^{-13} \text{ m}^2$$

Acknowledgements The work was supported by the Fundamental Research Funds for National Science and Technology Major Projects (2016ZX05011-002) and the Central Universities (2652015142). The kind effort from Dr. Y.Y Ziggah, Dr. A.A Eftekhari, Dr. K. Schüller, and Dr. X. Emery for their tireless assistance in carrying out this research. We also thank Mr. Bright Junior Addo for his kind assistance with fruitful and constructive criticism of this research paper. We would also like to thank the anonymous reviewers for their comments and suggestions that were helpful in improving the manuscript.

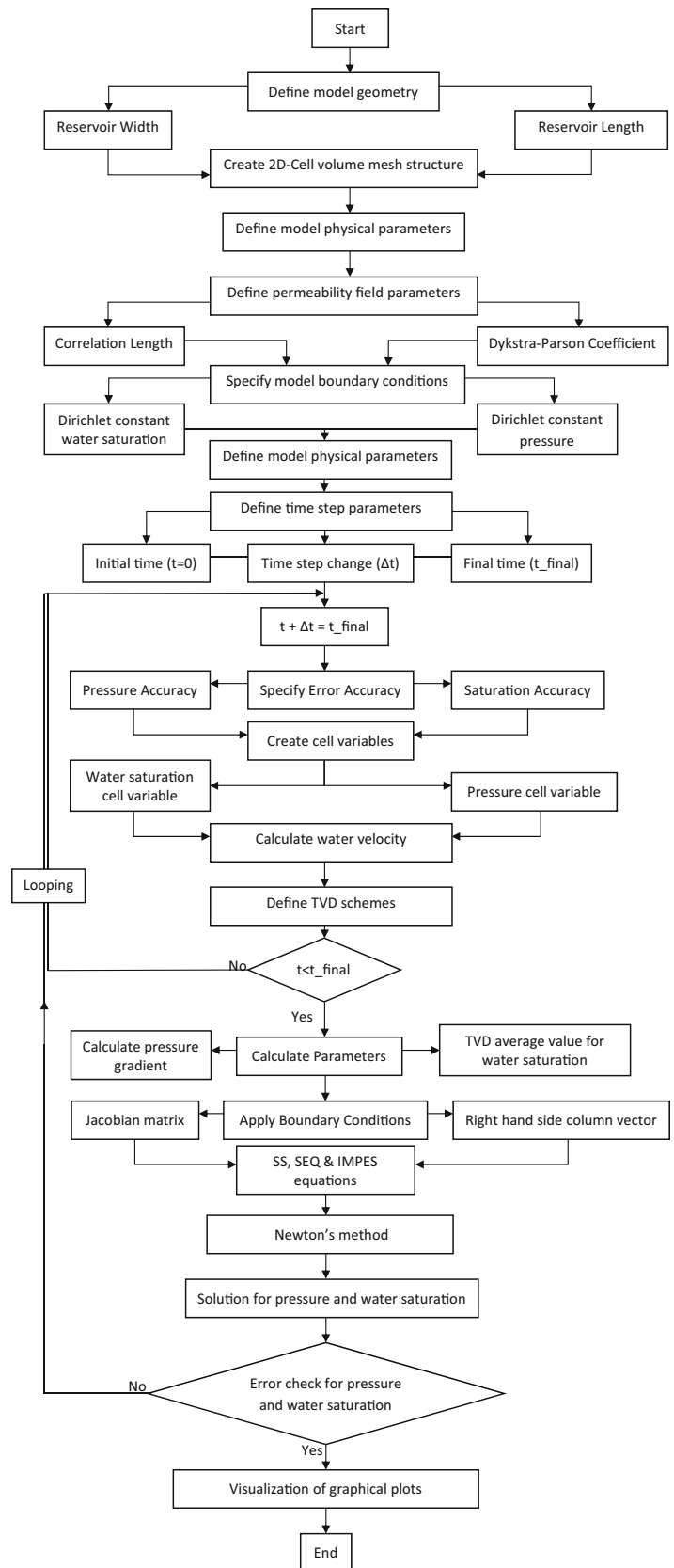
Compliance with ethical standards

Conflict of interest The authors declare that they have no conflicts of interest with respect to the research, authorship, and/or publication of this article.

Appendix

See Fig. 15.

Fig. 15 Computer modeling development flowchart



References

- Araktingi U, Orr F Jr (1993) Viscous fingering in heterogeneous porous media. *SPE Adv Technol Ser* 1(1):71
- Babaei M, Joekar-Niasar V (2016) A transport phase diagram for pore-level correlated porous media. *Adv Water Resour* 92:23–29
- Bergamashi N, Putti M (1999) Mixed finite elements and Newton-type linearization for the solution of Richards' equation. *Int J Numer Methods Eng* 45:1025–1046
- Bergström D (2012) MySimLabs. <http://www.mysimlabs.com/about.html>
- Bijeljic B, Raeini A, Mostaghimi P, Blunt MJ (2013) Predictions of non-Fickian solute transport in different classes of porous media using direct simulation on pore-scale images. *Phys Rev E* 87(1):013011
- Bouquet S, Leray S, Douarche F, Roggero F (2017) Characterization of viscous unstable flow in porous media at pilot scale-application to heavy oil polymer flooding. In: IOR 2017-19th European symposium on improved oil recovery
- Brantson ET, Ju B, Wu D (2018) Numerical simulation of viscous fingering and flow channeling phenomena in perturbed stochastic fields: finite volume approach with tracer injection tests. *Arab J Sci Eng*. <https://doi.org/10.1007/s13369-018-3070-0>
- Buckley SE, Leverett M (1942) Mechanism of fluid displacement in sands. *Trans AIME* 146(01):107–116
- Byer TJ (2000) Preconditioned newton methods for simulation of reservoirs with surface facilities. Department of Petroleum Engineering
- Chen Z (2007) Reservoir simulation: mathematical techniques in oil recovery. Society for Industrial and Applied Mathematics, pp 103–128. <https://doi.org/10.1137/1.9780898717075>
- Chen Z, Huan G, Ma Y (2006) Computational methods for multiphase flows in porous media. *Soc Ind Appl Math*
- Corey AT (1954) The interrelation between gas and oil relative permeabilities. *Prod Mon* 19(1):38–41
- Craig FG (1971) The reservoir engineering aspect of water of waterflooding. *SPE Monograph series*, Vol 3, Richardson, TX, pp 10–11
- Daripa P, Glimm J, Lindquist B, McBryan O (1988) Polymer floods: a case study of nonlinear wave analysis and of instability control in tertiary oil recovery. *SIAM J Appl Math* 48(2):353–373
- De Lucia M, Lagneau V, De Fouquet C, Bruno R (2011) The influence of spatial variability on 2D reactive transport simulations. *CR Geosci* 343(6):406–416
- Delamaide E (2014) Polymer flooding of heavy oil—from screening to full-field extension. In: *SPE heavy and extra heavy oil conference: Latin America*. Society of Petroleum Engineers
- Deutsch CV, Journel AG (1992) *GSLB: geostatistical software library and user's guide*. Oxford University Press, Oxford
- Doorwar S, Mohanty KK (2016) *Viscous-Fingering Function for Unstable Immiscible Flows*, University of Texas at Austin
- Douglas JJ, Peaceman DW, Rachford H.H (1959) A method for calculating multi-dimensional immiscible displacement. *Trans AIME* 216:297–306
- Dubrule O (1988) A review of stochastic models for petroleum reservoirs. Paper presented at the 1988 British Soc. Reservoir geologists meeting on quantification of sediment body geometries and their internal heterogeneities, London
- Dykstra H, Parsons RL (1950) The prediction of oil recovery by waterflood. *Second Recover Oil USA* 2:160–174
- Eftekhari AA, Schüller K (2015) FVTool: a finite volume toolbox for Matlab (Version v0.11). Zenodo. <http://doi.org/10.5281/zenodo.32745>
- Emery X, Lantuéjoul C (2006) Tbsim: a computer program for conditional simulation of three-dimensional gaussian random fields via the turning bands method. *Comput Geosci* 32(10):1615–1628
- Erandi DI, Wijeratne N, Britt M, Halvorsen BM (2015) Computational study of fingering phenomenon in heavy oil reservoir with water drive. *Fuel* 158:306–314. <https://doi.org/10.1016/j.fuel.2015.05.052>
- Farnstrom KL, Ertekin T (1987). A versatile, fully implicit, black oil simulator with variable bubble-point option. In: *SPE California regional meeting*. Society of Petroleum Engineers
- Freulon X, de Fouquet C (1991) Remarques sur la pratique des bandes tournantes a 3D. *Cahiers de Gostatistique, Fascicule 1*:101–117
- Garcia N, Stoll E (1984) Monte Carlo calculation for electromagnetic-wave scattering from random rough surfaces. *Phys Rev Lett* 52(20):1798
- Gneiting T (1999) Correlation functions for atmospheric data analysis. *Quart J R Meteorol Soc* 125(559):2449–2464
- Gotway CA, Rutherford BM (1994). Stochastic simulation for imaging spatial uncertainty: comparison and evaluation of available algorithms. In: *Geostatistical simulations*. Springer, Netherlands, pp 1–21
- Haddad RA, Akansu AN (1991) A class of fast Gaussian binomial filters for speech and image processing. *IEEE Trans Signal Process* 39(3):723–772
- Haldorsen HH, Damsleth E (1990) Stochastic Modeling (includes associated papers 21255 and 21299). *J Petrol Technol* 42(04):404–412
- Harten A (1983) High resolution schemes for hyperbolic conservation laws. *J Comput Phys* 49:357–393. <https://doi.org/10.1006/jcph.1997.5713> (**Bibcode:1997JCoPh. 135.260H**)
- Henderson N, Brëttes JC, Sacco WF (2015) Applicability of the three-parameter Kozeny–Carman generalized equation to the description of viscous fingering in simulations of waterflood in heterogeneous porous media. *Adv Eng Softw* 85:73–80
- Islam MR, Moussavizadegan SH, Mustafiz S, Abou-Kassem JH (2010) *Advanced petroleum reservoir simulation*. Wiley, Hoboken, p 277
- Johnson CE (1956) Production of oil recovery by water flood—a simplified graphical treatment of the Dykstra-Parsons method. *J Petr Tech Trans AIME* 207:345–346
- Journel AG, Huijbregts CJ (1978) *Mining geostatistics*. Academic Press, Cambridge
- Kalia N, Balakotaiah V (2009) Effect of medium heterogeneities on reactive dissolution of carbonates. *Chem Eng Sci* 64:376–390
- Knackstedt MA, Sheppard AP, Sahimi M (2001) Pore network modelling of two-phase flow in porous rock: the effect of correlated heterogeneity. *Adv Water Resour* 24(3):257–277
- Kou J, Sun S (2010) On iterative IMPES formulation for two-phase flow with capillarity in heterogeneous porous media. *Int J Numer Anal Model Ser B* 1(1):20–40
- Lacroix S, Vassilevski YV, Wheeler JA, Wheeler MF (2003) Iterative solution methods for modeling multiphase flow in porous media fully implicitly. *SIAM J Sci Comput* 25(3):905–926
- Lake LW, Malik MA (1993) Modelling fluid flow through geologically realistic media. *Geol Soc Lond Spec Publ* 73(1):367–375
- Leng CC (2013) The effect of spatial correlation on viscous fingering in a dynamic pore-network model with Delaunay tessellated structure (Master's thesis)
- Lie KA (2014) An introduction to reservoir simulation using MATLAB user guide for the MATLAB reservoir simulation toolbox (MRST). SINTEF ICT, Department of Applied Mathematics
- List F, Radu FA (2016) A study on iterative methods for solving Richards' equation. *Comput Geosci* 20(2):341–353
- Liu XD, Osher S, Chan T (1994) Weighted essentially non-oscillatory schemes. *J Comput Phys* 115(1):200–212

- Luo H, Delshad M, Pope GA, Mohanty KK (2017) Interactions between viscous fingering and channeling for unstable water/polymer floods in heavy oil reservoirs. In: SPE Reservoir simulation conference. Society of Petroleum Engineers
- MacDonald RC (1970) Methods for numerical simulation of water and gas coning. *Soc Petrol Eng J* 10(04):425–436
- Mantoglou A, Wilson JW (1982) The turning bands methods for simulation of random fields using line generation by a spectral method. *Water Res* 18(5):1379–1394
- Marcu GI (2004) Application of TVD flux limiting schemes in simulation of multiphase flow through porous media. The 6th international conference on hydraulic machinery and hydrodynamics Timisoara, Romania. pp 643–648
- Matheron G (1973) The intrinsic random functions and their applications. *Adv Appl Probab* 5(3):439–468
- MATLAB and Statistics Toolbox Release R (2016) The MathWorks, Inc., Natick, Massachusetts, United States
- Monteagudo JE, Firoozabadi A (2007a) Control-volume model for simulation of water injection in fractured media: incorporating matrix heterogeneity and reservoir wettability effects. *SPE J* 12(03):355–366
- Monteagudo JEP, Firoozabadi A (2007b) Comparison of fully implicit and IMPES formulations for simulation of water injection in fractured and unfractured media. *Int J Numer Meth Eng* 69(4):698–728
- Nixon MS, Aguado AS (2008) Feature extraction and image processing. Academic Press, Cambridge, p 88
- Pacheco TB, da Silva AFC, Maliska CR (2016) Comparison of IMPES, sequential, and fully implicit formulations for two-phase flow in porous media with the element-based finite volume method
- Radu FA, Pop IS, Knabner P (2006) On the convergence of the Newton method for the mixed finite element discretization of a class of degenerate parabolic equation. *Numerical Mathematics and Advanced Applications*, pp 1194–1200
- Radu FA, Suci N, Hoffmann J, Vogel A, Kolditz O, Park CH, Attinger S (2011) Accuracy of numerical simulations of contaminant transport in heterogeneous aquifers: a comparative study. *Adv Water Resour* 34(1):47–61
- Radu FA, Nordbotten JM, Pop IS, Kumar K (2015) A robust linearization scheme for finite volume based discretizations for simulation of two-phase flow in porous media. *J Comput Appl Math* 289:134–141
- Riaz A, Tchelepi HA (2006) Numerical simulation of immiscible two-phase flow in porous media. *Phys Fluids* 18(1):014104
- Roe PL (1985) Some contributions to the modeling of discontinuous flows, *Lectures in Applied Mechanics*, Vol. 22, Springer, Berlin, pp 163–193
- Rubin B, Blunt MJ (1991) Higher-order implicit flux limiting schemes for black oil simulation. Paper SPE 21222 presented at 11-th SPE symposium on reservoir simulation, Anaheim, pp. 219–228
- Sabelfeld KK (1991) Monte Carlo methods in boundary value problems. Springer, Berlin
- Shinozuka M, Jan CM (1972) Digital simulation of random processes and its applications. *J Sound Vib* 25(1):111–128
- Sweby PK (1984) High resolution schemes using flux limiters for hyperbolic conservation laws. *SIAM J Numer Ana006C* 21:995–1011
- Taggart IJ, Pinczewski WV (1985) The use of higher order differencing techniques in reservoir simulation. Paper resented at the sixth SPE symposium on reservoir simulation, Dallas, Texas
- Tompson AF, Ababou R, Gelhar LW (1989) Implementation of the three-dimensional turning bands random field generator. *Water Resour Res* 25(10):2227–2243
- Van Leer B (1979) Towards the ultimate conservative difference scheme. V. A second-order sequel to Godunov's method. *J Comput Phys* 32(1):101–136
- Versteeg HK, Malalasekera W (2007) An introduction to computational fluid dynamics: the finite, vol method. Pearson Education, London
- Watts JW, Shaw JS (2005) A new method for solving the implicit reservoir simulation matrix equation. In: SPE reservoir simulation symposium. Society of Petroleum Engineers
- Wendroff BLP (1960) Systems of conservation laws. *Commun Pure Appl Math* 13:217–237
- Willhite GP (1986) Waterflooding, SPE textbook series Vol. 3, Richardson, pp 1–2
- Zhang W, Al Kobaisi M (2017) A two-step finite volume method for the simulation of multiphase fluid flow in heterogeneous and anisotropic reservoirs. *J Petrol Sci Eng* 156:282–298
- Zhang JH, Liu ZH (1998) Study of the relationship between fractal dimension and viscosity ratio for viscous fingering with a modified DLA model. *J Petrol Sci Eng* 21(1):123–128